J. Fluid Mech. (1999), *vol.* 400, *pp.* 163–197. Printed in the United Kingdom

Examination of hypotheses in the Kolmogorov refined turbulence theory through high-resolution simulations. Part 2. Passive scalar field

By LIAN-PING WANG[1]†, SHIYI CHEN[2] AND JAMES G. BRASSEUR[3]

[1]Department of Mechanical Engineering,126 Spencer Laboratory, University of Delaware, Newark, DE 19716, USA

[2]Center for Nonlinear Studies and Theoretical Division, Los Alamos National Laboratory, Los Alamos, NM 87545, USA

[3]Department of Mechanical Engineering, Pennsylvania State University, University Park, PA 16802, USA

(Received 2 December 1998 and in revised form 6 July 1999)

Using direct numerical simulations (DNS) and large-eddy simulations (LES) of velocity and passive scalar in isotropic turbulence (up to 512^3 grid points), we examine *directly* and *quantitatively* the refined similarity hypotheses as applied to passive scalar fields (RSHP) with Prandtl number of order one. Unlike previous experimental investigations, exact energy and scalar dissipation rates were used and scaling exponents were quantified as a function of local Reynolds number. We first demonstrate that the forced DNS and LES scalar fields exhibit realistic inertial-range dynamics and that the statistical characteristics compare well with other numerical, theoretical and experimental studies. The Obukhov–Corrsin constant for the $k^{-5/3}$ scalar variance spectrum obtained from the 512^3 mesh is 0.87 ± 0.10. Various statistics indicated that the scalar field is more intermittent than the velocity field. The joint probability distribution of locally-averaged energy dissipation ϵ_r and scalar dissipation χ_r is close to log-normal with a correlation coefficient of 0.25 ± 0.01 between the logarithmic dissipations in the inertial subrange. The intermittency parameter for scalar dissipation is estimated to be in the range $0.43 \sim 0.77$, based on direct calculations of the variance of $\ln \chi_r$. The scaling exponents of the conditional scalar increment $\overline{\delta_r\theta|_{\chi_r,\epsilon_r}}$ suggest a tendency to follow RSHP. Most significantly, the scaling exponent of $\overline{\delta_r\theta|_{\chi_r,\epsilon_r}}$ over ϵ_r was shown to be approximately $-\frac{1}{6}$ in the inertial subrange, confirming a dynamical aspect of RSHP. In agreement with recent experimental results (Zhu *et al.* 1995; Stolovitzky *et al.* 1995), the probability distributions of the random variable $\beta_s = \delta_r\theta|_{\chi_r,\epsilon_r}/(\chi_r^{1/2}\epsilon_r^{-1/6}r^{1/3})$ were found to be nearly Gaussian. However, contrary to the experimental results, we find that the moments of β_s are almost identical to those for the velocity field found in Part 1 of this study (Wang *et al.* 1996) and are insensitive to Reynolds number, large-scale forcing, and subgrid modelling.

† Author to whom correspondence should be addressed: e-mail: lwang@me.udel.edu.

1. Introduction

Progress in characterizing turbulence structure is limited by the complexity associated with strong nonlinear couplings over a wide range of scales. The separation of scales at high Reynolds numbers makes it fruitful to study the structure of turbulence in a scale-space description. A simplification of a scale-space description of turbulence was made by Kolmogorov (1941*a*, *b*, referred to herein as K41), who related the statistics of velocity increments to the average dissipation rate of kinetic energy $\bar{\epsilon}$ based on a model of local energy cascade and dimensional arguments. This K41 theory was later extended to account for strong intermittency in local energy dissipation rate by Obukhov (1962) and Kolmogorov (1962), now known as the K62 refined turbulence theory. Both the K41 and K62 theories lead to predictions of scaling parameters in high Reynolds number turbulence, some of which have been confirmed experimentally (e.g. Monin & Yaglom 1975; Anselmet *et al.* 1984; Meneveau & Sreenivasan 1991).

The K62 theory was based on a set of *refined similarity* hypotheses (RSH). Direct examinations of these hypotheses have been carried out experimentally (Stolovitzky, Kailasnath & Sreenivasan 1992; Praskovsky 1992; Thoroddsen & Van Atta 1992*a*; Zhu, Antonia & Hosokawa 1995) and numerically (Hosokawa & Yamamoto 1992; Chen *et al.* 1993; Wang *et al.* 1996).

In Part 1 of this work (Wang *et al.* 1996), we examined in detail the refined hypotheses, using direct numerical simulation (DNS) and large-eddy simulation (LES) data and measured scaling exponents over the local scale r and the locally-averaged dissipation rate ϵ_r of kinetic energy. Although the transverse Taylor-microscale Reynolds number of the DNS flows was about 200, the scale-dependent Reynolds number R_{ϵ_r} (to be defined later in this section) was sufficient to identify an inertial range and measure *universal* constants in the K62 theory. Two significant observations were made. First, like Kraichnan (1974*a*), we argued that absolute values should be placed around velocity differences. Second, the K62 theory is better realized when the full kinetic-energy dissipation rate is used rather than the one-dimensional surrogate necessarily used in experimental studies. This point was also made by Hosokawa & Oide (1996). It has recently been observed that transverse velocity increments probably follow a different scaling than longitudinal velocity increments at finite Reynolds numbers (Boratav & Pelz 1997; Grossmann, Lohse & Reeh 1997; Camussi & Benzi 1997; Chen *et al.* 1997; Dhruva, Tsuji & Sreenivasan 1997). It has been suggested (Chen *et al.* 1997) that transverse velocity increments scale better using locally averaged enstrophy rather than locally averaged dissipation rate.

Turbulence enhances mixing through the generation of small-scale scalar fluctuations, distortion of scalar interfaces, and creation of intermittent large scalar gradients at very small scales, enhancing subsequent diffusive mixing at the molecular level. The K41 similarity theory for turbulent velocity was extended to passive scalar by Obukhov (1949), Yaglom (1949), and Corrsin (1951). Complications resulting from non-unity Prandtl (or Schmidt) numbers were treated by Batchelor (1959) and Batchelor, Howells & Townsend (1959). The RSH can be extended to scalars by considering fluctuations in both local energy dissipation and scalar dissipation rates.

Analyses of the refined similarity hypotheses for passive scalar (RSHP) are given by Monin & Yaglom (1975), Van Atta (1971), and Antonia & Van Atta (1975). Antonia *et al.* (1984) compiled measurements of power-law exponents for temperature structure functions up to $n = 12$ and found that both the log-normal (Van Atta 1971) and the β (Frisch, Sulem & Nelkin 1978) models are unsatisfactory. The scaling

theory for passive scalar fluctuations is further developed in Meneveau *et al.* (1990) using a joint multifractal formulation of two fluctuating dissipation rate fields. They obtained intermittency parameters for the dissipation fields and correlation coefficients between the logarithm of scalar and energy dissipation rates. Starting from RSHP, Hosokawa (1994) devised an analytical model for the probability distribution of scalar increments and scalar gradient which shows good agreement with the experimental data of Antonia *et al.* (1984) and Thoroddsen & Van Atta (1992*b*). Scaling exponents based on RSHP and a joint log-Poisson model have been developed by Cao & Chen (1997).

Direct examinations of RSHP using experimental data were made by Zhu *et al.* (1995) and Stolovitzky, Kailasnath & Sreenivasan (1995). Before summarizing these studies, however, we first describe the Obukhov–Yaglom–Corrsin theory, RSHP, and our notation. We focus in this study on the case of $Pr \approx 1$, as in Zhu *et al.* (1995) and Stolovitzky *et al.* (1995).

1.1. *Summary of the Obukhov–Yaglom–Corrsin theory and RSHP*

Let L_s be the integral scale of the passive scalar field $\theta(\boldsymbol{x}, t)$, which is usually comparable to the integral scale L_f of the velocity field. When applied to a passive scalar, the first hypothesis of Obukhov–Yaglom–Corrsin theory states that the distribution of the scalar difference, $\Delta_r\theta \equiv \theta(\boldsymbol{x}+\boldsymbol{r}, t)-\theta(\boldsymbol{x}, t)$, between two points in space is uniquely determined by a local length scale $r \equiv |\boldsymbol{r}|$ where $r \ll L_\theta$, ν, D, $\bar{\epsilon}$, and the mean rate of dissipation of scalar variance per unit mass $\bar{\chi}$. Here a bar over a quantity implies an ensemble average. If the scalar field is locally isotropic at the scale r, then statistics of $\Delta_r\theta$ are independent of the orientation of $\boldsymbol{r}$. The energy and scalar dissipation rates are given by

$$\epsilon(\boldsymbol{x}, t) = \frac{\nu}{2}\left(\frac{\partial u_i}{\partial x_j}+\frac{\partial u_j}{\partial x_i}\right)\left(\frac{\partial u_i}{\partial x_j}+\frac{\partial u_j}{\partial x_i}\right), \quad \chi = 2D\frac{\partial\theta}{\partial x_i}\frac{\partial\theta}{\partial x_i}, \tag{1.1}$$

where $u_i(\boldsymbol{x}, t)$ and $\theta(\boldsymbol{x}, t)$ are the velocity and scalar fields, respectively. The one-dimensional surrogates of ϵ and χ are $\epsilon' = 15\nu(\partial u_1/\partial x_1)^2$ and $\chi' = 6D(\partial\theta/\partial x_1)^2$. The prime will also be used for quantities derived from ϵ' and χ'. The K41 type of scaling implies that the moments of $\delta_r\theta \equiv |\Delta_r\theta|$ are given by

$$\overline{(\delta_r\theta)^n} = (\bar{\chi}^{1/2}\,\bar{\epsilon}^{-1/6}\,r^{1/3})^n F_n(R_r, Pr), \tag{1.2}$$

where $R_r = \bar{\epsilon}^{1/3}\,r^{4/3}/\nu = (r/\eta)^{4/3}$ is a local Reynolds number at scale r with local velocity scale $(\bar{\epsilon}r)^{1/3}$ and Kolmogorov scale $\eta = (\nu^3/\bar{\epsilon})^{1/4}$. $F_n(R_r, Pr)$ are universal functions at high global Reynolds numbers, $R_\lambda = \lambda u_{rms}/\nu$, where $\lambda \equiv (15\nu u_{rms}^2/\bar{\epsilon})^{1/2}$ and u_{rms} are the transverse Taylor microscale and r.m.s. component fluctuation velocity, respectively.

Equation (1.2) with $n = 2$ implies that a universal scalar variance spectrum $G(k)$ exists at high wavenumbers such that

$$\frac{G(k)}{(\bar{\chi}/\bar{\epsilon})(\bar{\epsilon}\nu^5)^{1/4}} = (k\eta)^{-5/3}\psi(k\eta, Pr). \tag{1.3}$$

The more specific Batchelor scaling assumes that the scalar field is affected by the velocity field only through the mean rate of strain $(\bar{\epsilon}/\nu)^{0.5}$ and (1.3) reduces to

$$\frac{G(k)}{\bar{\chi}\eta_B(\nu/\bar{\epsilon})^{1/2}} = (k\eta_B)^{-5/3}\psi_B(k\eta_B), \tag{1.4}$$

where the Batchelor scale $\eta_B \equiv (\nu D^2/\bar{\epsilon})^{1/4}$.

Kolmogorov's second similarity hypothesis for a scalar field states that when $R_r \gg 1$ (i.e. $r \gg \eta$ or $k \ll \eta^{-1}$ and $r \ll L_s, L_f$), the distribution of the normalized scalar difference $\delta_r\theta/(\overline{\chi}^{1/2}\,\overline{\epsilon}^{-1/6}\,r^{1/3})$ becomes independent of ν and D. It follows that in this *inertial subrange*,

$$\overline{(\delta_r\theta)^n} = H_n(\overline{\chi}^{1/2}\,\overline{\epsilon}^{-1/6}\,r^{1/3})^n, \tag{1.5}$$

where H_n are universal constants. In particular, when $n = 2$, (1.5) implies the well-known scalar variance spectrum for the inertial subrange,

$$G(k) = C_s\overline{\chi}\overline{\epsilon}^{-1/3}k^{-5/3}, \tag{1.6}$$

where C_s is the Obukhov–Corrsin constant, and $C_s = 0.4H_2$ (Monin & Yaglom 1975, p. 385). The $k^{-5/3}$ scalar variance spectrum has been observed in numerous experiments (see Monin & Yaglom 1975, pp. 499–501; Jayesh, Tong & Warhaft 1994), suggesting that any intermittency correction under the RSHP is very small. The higher-order moments of the scalar increments ($n > 2$) do not agree with the above K41 formulation due to the intermittent fluctuations of the two dissipation fields χ and ϵ (e.g. Mydlarski & Warhaft 1998).

In analogy to the refined formulation of Kolmogorov–Obuhkov (1962) for the velocity increments, a refined formulation for scalar increments can be made (e.g. Monin & Yaglom 1975; Van Atta 1971). The locally volume-averaged dissipation rates over spheres of diameter r are

$$\chi_r(\boldsymbol{x},t) = \frac{6}{\pi r^3}\int_{|\boldsymbol{h}|\leqslant r/2}\chi(\boldsymbol{x}+\boldsymbol{h},t)\mathrm{d}\boldsymbol{h}, \quad \epsilon_r(\boldsymbol{x},t) = \frac{6}{\pi r^3}\int_{|\boldsymbol{h}|\leqslant r/2}\epsilon(\boldsymbol{x}+\boldsymbol{h},t)\mathrm{d}\boldsymbol{h}. \tag{1.7}$$

The first part of the refined turbulence theory assumes that the probability distribution of (χ_r, ϵ_r) is jointly log-normal in the inertial subrange, i.e.

$$f(\chi_r,\epsilon_r) = \frac{1}{2\pi\sigma_r\pi_r\sqrt{1-\rho_r^2}}\frac{1}{\chi_r\epsilon_r}\exp\left\{-\frac{1}{2(1-\rho_r^2)}\left[\frac{(\ln\chi_r - b_r)^2}{\pi_r^2}\right.\right.$$
$$\left.\left. - 2\rho_r\frac{(\ln\chi_r - b_r)}{\pi_r}\frac{(\ln\epsilon_r - m_r)}{\sigma_r} + \frac{(\ln\epsilon_r - m_r)^2}{\sigma_r^2}\right]\right\}, \tag{1.8}$$

where $b_r = \overline{\ln\chi_r}$, $m_r = \overline{\ln\epsilon_r}$, and π_r and σ_r are standard deviations of $\ln\chi_r$ and $\ln\epsilon_r$, respectively. The correlation coefficient ρ_r is

$$\rho_r = \frac{\overline{(\ln\chi_r - b_r)(\ln\epsilon_r - m_r)}}{\pi_r\sigma_r}. \tag{1.9}$$

In addition the theory assumes that the variances follow the scalings

$$\pi_r^2 = A_s + \mu_s\ln\frac{L}{r}, \quad \sigma_r^2 = A + \mu\ln\frac{L_f}{r}, \tag{1.10}$$

where μ_s and μ are theoretically universal *intermittency parameters*, the constants A_s and A depend on flow geometry, and $L = \min(L_f, L_s)$.

The refined similarity hypotheses (RSHP) are specified separately from the assumed log-normality of dissipation fluctuations (e.g. Stolovitzky *et al.* 1995). The first hypothesis relates the moments of $\delta_r\theta$ conditioned on both χ_r and ϵ_r to ν, D, χ_r, ϵ_r, and r, in a manner analogous to (1.2),

$$\overline{(\delta_r\theta)^n|_{\chi_r,\epsilon_r}} = (\chi_r^{1/2}\,\epsilon_r^{-1/6}\,r^{1/3})^n\,P_n(R_{\epsilon_r}, Pr) \quad \text{for } r \ll L, \tag{1.11}$$

where $P_n(R_{\epsilon_r}, Pr)$ are hypothesized to be universal functions of a *new local Reynolds*

number $R_{\epsilon_r} = \epsilon_r^{1/3} r^{4/3}/\nu$ and the Prandtl number. In spatially homogeneous flows, the conditional expectation is calculated based on a subset of spatial regions where both χ_r and ϵ_r are fixed. A more general statement of this RSHP is that the probability distribution of the normalized scalar increment

$$\beta_s \equiv \frac{\delta_r\theta|_{\chi_r,\epsilon_r}}{\chi_r^{1/2}\,\epsilon_r^{-1/6}\,r^{1/3}}, \tag{1.12}$$

is a universal function of R_{ϵ_r} and Pr. The corresponding random variable for the velocity field is $\beta \equiv \delta_r u|_{\epsilon_r}/(\epsilon_r r)^{1/3}$ with $\delta_r u$ being the longitudinal velocity increment. The corresponding variables when the one-dimensional surrogates of dissipation rates are used will be denoted by β_s' and β'.

The second refined similarity hypothesis states that when $R_{\epsilon_r} \gg 1$ and $Pr \sim 1$, the function $P_n(R_{\epsilon_r}, Pr)$ has asymptotic value. Therefore,

$$\overline{(\delta_r\theta)^n|_{\chi_r,\epsilon_r}} = W_n(\chi_r^{1/2}\,\epsilon_r^{-1/6}\,r^{1/3})^n, \tag{1.13}$$

where W_n are universal constants and the probability distribution of β_s takes a universal form independent of R_{ϵ_r} and Pr.

Taylor expansion in the limit of $r/\eta \to 0$ gives

$$\overline{(\delta_r\theta)^2|_{\chi_r,\epsilon_r}} \sim \overline{\left(\frac{\partial\theta}{\partial x}\right)^2} r^2 = \frac{1}{6}\left(\frac{\chi_r}{D}\right) r^2, \tag{1.14}$$

which is consistent with the first RSHP, equation (1.11), when $P_2 = Pr\,R_{\epsilon_r}/6$. More generally,

$$\overline{(\delta_r\theta)^n|_{\chi_r,\epsilon_r}} \sim \left(\frac{\chi_r}{D}\right)^{n/2} r^n \quad \text{as } r/\eta \to 0. \tag{1.15}$$

1.2. *Analysis of RSHP*

Zhu *et al.* (1995) examined in some detail RSHP experimentally in a circular jet at $R_\lambda = 250$, and in the atmospheric surface layer at $R_\lambda = 7200$. In both experiments $Pr = 0.7$ (air). They examined qualitatively the scaling exponents of scalar increments, and mixed scalar–velocity increments over combined variables $x' \equiv (r\epsilon_r')^{1/3}$ and $x_s' \equiv r^{1/3}\,\epsilon_r'^{\,-1/6}\,\chi_r'^{\,1/2}$ using the one-dimensional surrogates. They found that the statistics of β' and β_s' were not independent of the local scale r even in the inertial subrange. Nevertheless, they found that, in agreement with RSHP, the conditional p.d.f.s of β' and β_s' appear to be nearly independent of local Reynolds number $R_{\epsilon_r'}$ when $R_{\epsilon_r'} \gtrsim 50$ and the distributions are nearly Gaussian.

Stolovitzky *et al.* (1995) rationalized the r-dependence of the random variables β' and β_s' in the inertial subrange and proposed a modified version of RSHP in terms of ϵ_r' and χ_r'. With a new assumption of local isotropy, they derived a refined Yaglom equation for $\overline{\Delta_r u(\Delta_r\theta)^2|_{\chi_r',\epsilon_r'}}$. In a wake flow behind a heated cylinder at $R_\lambda = 160$ and $Pr = 0.7$, they found experimentally that p.d.f.s of the random variable β_s' for large $R_{\epsilon_r'}$ were nearly Gaussian. They also observed a linear dependence on r of the conditional expectation $\overline{\Delta_r u(\Delta_r\theta)^2|_{\chi_r',\epsilon_r'}}$. They remarked that 'it would be highly desirable that similar tests be performed using DNS of passive scalars mixed by turbulence, considering the full expression for both dissipation rates'.

Mydlarski & Warhaft (1998) reported conditional passive scalar statistics in nearly isotropic grid turbulence for R_λ up to 731. They observed an almost linear dependence of $\delta_r\theta|_{x_s'}$ on x_s', in agreement with RSHP. However, they did not observe the expected correlation between the energy dissipation rate ϵ_r' and the temperature increment in the inertial subrange.

The difficulties specific to direct examinations of RSHP are worth emphasizing. In DNS, the Reynolds numbers are moderate and the inertial subrange, if it exists, is very narrow in the scale space. On the other hand, even when R_λ is moderate, the local Reynolds number R_{ϵ_r} extends over a much wider range and certain small-scale features of turbulence approach their asymptotic state (Part 1). As we pointed out in Part 1, there are significant advantages in numerical experiments, which makes it useful to conduct a careful study of RSH even with moderate Reynolds numbers. The first is the access to the exact local dissipation rates. The second is the accurate evaluation of spatial derivatives and the use of spatial averages in homogeneous turbulence and consequent accurate statistics of conditional quantities.

In physical experiments (Meneveau *et al.* 1990; Zhu *et al.* 1995; Stolovitzky *et al.* 1995), the one-dimensional surrogates of dissipation rates are necessarily analysed in place of the full dissipation rates, and Taylor's frozen flow hypothesis is invoked to measure spatial derivatives from time derivatives. Furthermore, the temperature probe and the velocity probe have to be separated by a finite distance to avoid mutual interferences.

1.3. *Objective*

Our main objective is to test RSHP, using exact dissipation rates accessible in our DNS flow fields. The scaling exponents will be quantified as a function of local Reynolds number. The question of whether universal moments of β_s exist will be studied.

General features of the isotropic, homogeneous turbulent scalar fields from high-resolution simulations are presented and compared with experimental observations in § 2. In § 3 we examine the probability distribution of χ_r and the joint distribution of χ_r and ϵ_r, as functions of both the spatial scale r and the local Reynolds number. We then study in § 4 the RSHP directly by quantifying the scaling exponents over χ_r, ϵ_r, and r. We also analyse the universal constants W_n in (1.13) and the probability distribution of β_s. In addition, we consider throughout the paper the use of large-eddy simulation, in which the dissipative scales are modelled, in examining RSHP in the inertial range of scales.

2. Analysis of the high-resolution simulation scalar fields

In this section, we describe the various scalar fields we used to study the refined turbulence theory for passive scalar fields. The simulations were performed on a 512-node CM-5 at Los Alamos National Laboratory. The velocity fields were identical to those described in Part 1. Therefore, we shall focus on the description of scalar field characteristics.

2.1. *Simulation method*

In addition to the velocity field solved by numerically integrating the Navier–Stokes equations and the continuity equation, the advection–diffusion equation for a passive scalar field $\theta(\boldsymbol{x}, t)$

$$\frac{\partial \theta}{\partial t} + \frac{\partial (\theta u_i)}{\partial x_i} = D \frac{\partial^2 \theta}{\partial x_i \partial x_i}, \tag{2.1}$$

was solved simultaneously on a cube of side $L_B = 2\pi$ using a standard pseudospectral algorithm, with periodic boundary conditions in the three coordinate directions. The flow domain is discretized uniformly into N^3 grid points, which defines the

wavenumber components in Fourier space as $k_j = \pm n_j(2\pi/L_B) = \pm n_j$, where $n_j = 0, 1, \ldots N/2 - 1$ for $j = 1, 2, 3$. A small portion of the velocity and scalar fields at higher wavenumbers, $k > k_{max}$ with $k_{max} = N\sqrt{2}/3$, is truncated at each time step to reduce aliasing errors.

Table 1 lists all the different scalar fields used in this study; the fields are identified with the same names as in Part 1 and the corresponding velocity field statistics can be found in table 1 therein. Both freely decaying and forced stationary isotropic turbulence fields were simulated. The freely decaying flows (d256c1 and d256c2) were generated from a previously developed forced stationary turbulence. The forced isotropic fields (f128, f256, and f512) were generated by applying forcings to both velocity and scalar fields in the wavenumber space at $k < 3$, to maintain kinetic energy and scalar variance spectra in the first two shells consistent with $k^{-5/3}$. This produces statistically stationary velocity and scalar fields with a more extensive nominal $k^{-5/3}$ inertial range and higher global flow Reynolds number, compared with the freely decaying turbulence. The forcing, however, introduces artifacts to the large-scale fluid motions which may affect the structure and internal similarity scaling near the forcing scales. Thus only wavenumber bands larger than these forced bands are used for scaling analyses in this paper.

The spatial resolution of a spectral simulation is often monitored by the value of $k_{max}\eta$, which should be greater than 1 for the smallest scales of the flow velocity to be resolved (Eswaran & Pope 1988*a*). This also ensures adequate resolution for the scalar field of $Pr \leqslant 1$. Since the scalar fields are somewhat more intermittent and the smallest scale in the scalar field is a factor of 0.64 smaller than the velocity field (see § 2.2 below), we typically use $k_{max}\eta > 1.4$ for passive scalar simulations of $Pr \leqslant 1$.

The Fourier coefficients of the velocity and scalar fields were advanced in time using a second-order Adams–Bashforth method for the nonlinear terms and an exact integration for the diffusion terms (Chen & Shan 1992). The time step was chosen to ensure that the Courant number was 0.4 or less for numerical stability and accuracy (Eswaran & Pope 1988*a*).

The inertial range in the DNS fields is necessarily very narrow because the maximum scale separation is limited by the grid resolution. To extend the inertial subrange, we also made use of a scalar field (les256) generated by moving the smallest inertial scales to higher wavenumbers through large-eddy simulation (LES). We modelled the scales below the grid spacing (filter scale) in both the velocity and scalar fields, using the subgrid scale (SGS) closure scheme of Métais & Lesier (1992). We also apply the same forcing method to the first two wavenumber shells to maintain the energy and scalar fluctuations in the resolved fields of the LES, thus moving the large-scale side of the inertial range to the lowest possible wavenumbers.

2.2. *Statistical characteristics of the scalar fields*

Here we shall document important statistics of the scalar fields for later discussions. We shall also demonstrate that realistic turbulent scalar fields are simulated by making various comparisons with known numerical, experimental, and theoretical results.

In table 1 we compile scalar field statistics. The first 15 quantities shown in the table (from top to bottom) are (dimensional variables are given in arbitrary units): the r.m.s. scalar fluctuation θ_{rms}, the average dissipation rate $\overline{\chi}$ of scalar variance, the scalar diffusivity D, Taylor-microscale Reynolds number $R_\lambda \equiv u_{rms}\lambda/\nu$, Prandtl number, the third-order mixed-derivative skewness, the flatness of the scalar derivative, the Batchelor scale, Corrsin microscale, scalar integral scale, the longitudinal integral length scale L_f of velocity, the two dimensionless scalar dissipation rates, and ratios

Simulation	d256c1	d256c2	f128	f256	f512	LES256	Experiment	Experiment
Grid	256^3	256^3	128^3	256^3	512^3	256^3	SAD77[a]	MW98[b]
Plot symbol	□	■	▽	○	●	◇		
θ_{rms}	0.766	0.141	1.09	1.09	1.10	1.04	—	0.580
$\overline{\chi}$	0.3449	0.004424	0.4190	0.4400	0.5012	0.3843[c]	—	0.581
D	1.429×10^{-3}	1.429×10^{-3}	0.004	0.002	0.001	7.48×10^{-4}[d]	—	22.1×10^{-6}
R_λ	132	68.1	100	151	195	—	175	247
Pr	0.7	0.7	1.0	1.0	1.0	0.58[e]	0.71	0.707
$\dfrac{\overline{(\partial u/\partial x)(\partial\theta/\partial x)^2}}{\overline{(\partial u/\partial x)^2}^{1/2}\,\overline{(\partial\theta/\partial x)^2}}$	−0.446	−0.493	−0.480	−0.477	−0.490	—	—	−0.451
$\dfrac{\overline{(\partial\theta/\partial x)^4}}{\left(\overline{(\partial\theta/\partial x)^2}\right)^2}$	11.3	10.4	11.7	16.8	13.8	—	7.0 ∼ 10.9	25.4
η_B	0.0103	0.0196	0.0490	0.0245	0.0122	6.02×10^{-3}	—	—
λ_s[f]	0.121	0.196	0.260	0.180	0.121	—	—	—
L_s[f]	0.752	0.883	0.956	0.937	0.918	1.00	—	—
L_f	1.072	1.049	1.530	1.514	1.412	1.470	—	—
$\overline{\chi}L_f/u_{rms}\theta_{rms}^2$	0.932	0.912	0.630	0.656	0.669	0.610	—	—
$\overline{\chi}u_{rms}^2/\overline{\epsilon}\theta_{rms}^2$	1.49	1.06	1.28	1.53	1.33	1.40	—	—
L_s/L_f	0.701	0.842	0.625	0.619	0.650	0.680	—	—
λ_s/λ	0.617	0.737	0.556	0.511	0.555	—	—	
$\dfrac{\overline{(\partial\theta/\partial y)^2}^{1/2}}{\overline{(\partial\theta/\partial x)^2}^{1/2}}$	1.003	1.001	0.960	0.985	1.023	—	1.07	1.0
$\dfrac{\overline{(\partial\theta/\partial z)^2}^{1/2}}{\overline{(\partial\theta/\partial x)^2}^{1/2}}$	0.987	1.025	1.012	1.038	0.995	—	1.21	1.2
$\dfrac{\overline{\xi^2}^{1/2}}{\overline{\chi}}$[g]	2.31	2.20	2.36	2.92	2.58	—	—	
S_ξ[g]	7.10	6.77	7.59	9.29	7.50	—	2.95	18.3
F_ξ[g]	89.5	93.3	99.5	140.0	95.8	—	19.96	586.0
$\dfrac{-\overline{g_ig_js_{ij}}}{\overline{g^2}\,\overline{(s_{ij}s_{ij})}^{1/2}}$[h]	0.409	0.461	0.448	0.440	0.459	—	—	—
β[i]	0.53	0.48	0.49	0.50	0.51	—	—	—

[a] Sreenivasan *et al.* (1977) in the inner region of a fully developed turbulent boundary layer at $y/\delta = 0.24$, where δ is the velocity boundary layer thickness. The full scalar dissipation rate χ was measured.

[b] Mydlarski & Warhaft (1998) for grid-generated scalar turbulence. Only the pseudo-scalar dissipation rate χ' was measured. The °C-m-s unit system is used.

[c] This number is computed as the total scalar variance flux across the filter cut-off.

[d] Effective diffusivity, see §4.

[e] Computed based on effective viscosity and diffusivity, see §4.

[f] Computed as: $\lambda_s = \sqrt{6D\theta_{rms}^2/\overline{\chi}}$; $L_s = \pi/(2\theta_{rms}^2)\int_0^\infty \mathrm{d}k\ G(k)/k$.

[g] $\xi \equiv \chi - \overline{\chi}$, S_ξ and F_ξ are skewness and flatness factor of ξ, respectively.

[h] $g_i = \partial\theta/\partial x_i$.

[i] The ratio between two normalized production terms, $\beta \equiv \left(\dfrac{\overline{\omega_i\omega_j s_{ij}}}{\overline{\omega^2}\,\overline{(s_{ij}s_{ij})}^{1/2}}\right)\Big/\left(\dfrac{-\overline{g_ig_js_{ij}}}{\overline{g^2}\,\overline{(s_{ij}s_{ij})}^{1/2}}\right)$.

TABLE 1. Scalar field characteristics from the simulations. Note that the symbols are used consistently throughout the paper to identify specific fields.

of integral lengths and Taylor microscales between the scalar and velocity fields. Note that the mixed-derivative skewness is close to -0.5 and almost independent of flow Reynolds number. The flatness of the scalar derivative is much higher (by a factor of 2 to 3) than the flatness of the velocity derivative shown in Part 1. These observations are in good agreement with previous numerical (e.g. Kerr 1985) and experimental (Antonia & Van Atta 1978; Antonia & Chambers 1980) results, although experiments typically show a slightly larger value (-0.52 to -0.62 at $R_\lambda \approx 10^4$ or higher) and a very weak Reynolds-number dependence for the mixed-derivative skewness (Antonia & Chambers 1980; Sreenivasan & Antonia 1997), possibly due to the inhomogeneity and isotropy of the experimental flows. The integral length scale was computed from the three-dimensional scalar variance spectrum $G(k)$:

$$L_s = \frac{\pi}{2\theta_{rms}^2} \int_0^\infty \frac{G(k)}{k}\,\mathrm{d}k, \tag{2.2}$$

where the scalar variance spectrum $G(k)$ is defined such that

$$\theta_{rms}^2 = \int_0^\infty G(k)\,\mathrm{d}k. \tag{2.3}$$

The spectrum was calculated by dividing wavenumber space into $N/2$ shells centred on radius k and with unit bin width $\Delta k = 1$, and then summing the modal scalar variance in each shell. The spatially averaged dissipation rate $\overline{\chi}$ is related to the scalar variance spectrum $G(k)$ by

$$\overline{\chi} \equiv 2D\overline{\frac{\partial\theta}{\partial x_j}\frac{\partial\theta}{\partial x_j}} = 2D\int_0^\infty k^2 G(k)\,\mathrm{d}k. \tag{2.4}$$

Table 1 shows that the average scalar dissipation rate $\overline{\chi}$ appears to be scaled better by $\overline{\epsilon}\theta_{rms}^2/u_{rms}^2$ than by $\theta_{rms}^2 u_{rms}/L_f$. Equivalently, we may state that the two dissipation-rate time scales, $u_{rms}^2/\overline{\epsilon}$ and $\theta_{rms}^2/\overline{\chi}$, are simply proportional. The same observation was made by Ashurst *et al.* (1987). Excluding the lowest R_λ case (d256c2), the four other DNS fields yield $\overline{\chi} = (1.40 \pm 0.10)\overline{\epsilon}\theta_{rms}^2/u_{rms}^2$. Furthermore, if $\overline{\chi}$ and $\overline{\epsilon}$ are replaced by the flux of scalar variance and kinetic energy in the LES, we obtain $\overline{\chi} = 1.40\overline{\epsilon}\theta_{rms}^2/u_{rms}^2$, in excellent agreement with the scaling for the DNS scalar fields. The two ratios, L_s/L_f and λ_s/λ, depend somewhat on large-scale structures, with the decaying flows giving a larger value than the forced flows. The Taylor microscale of the scalar field is about 30% to 45% smaller than that of the velocity field.

Figure 1(*a*) shows log-log plots of normalized three-dimensional scalar variance spectra for the various DNS scalar fields pre-multiplied by $k^{5/3}$ so that an inertial range, if there is one, would appear as a region of zero slope. Several observations can be made from this figure. First, with the exception of the lowest-R_λ d256c2 field, the energy spectra for different R_λ show a very good collapse almost over all wavenumbers, consistent with previous numerical results (Kerr 1990; Sullivan, Mahalingam & Kerr 1994; Pumir 1994). Second, there appears to be a bump near the energy dissipation peak, leading to a maximum value of 1.3 at $k\eta_B = 0.2$. The bump in the scalar spectrum is well-known (e.g. Hill 1978; Mydlarski & Warhaft 1998). Tatarskii *et al.* (1992) developed an asymptotic theory which shows the appearance of a bump in the scalar variance spectrum near the dissipation peak for a Prandtl number of approximately 1. Finally, the highest-R_λ f512 field shows a tendency towards an inertial range for $k\eta_B < 0.05$, with an average Obukhov–Corrsin constant of $C_s = 0.75 \pm 0.15$.

In figure 1(*b*) we show the normalized one-dimensional scalar variance spectra,

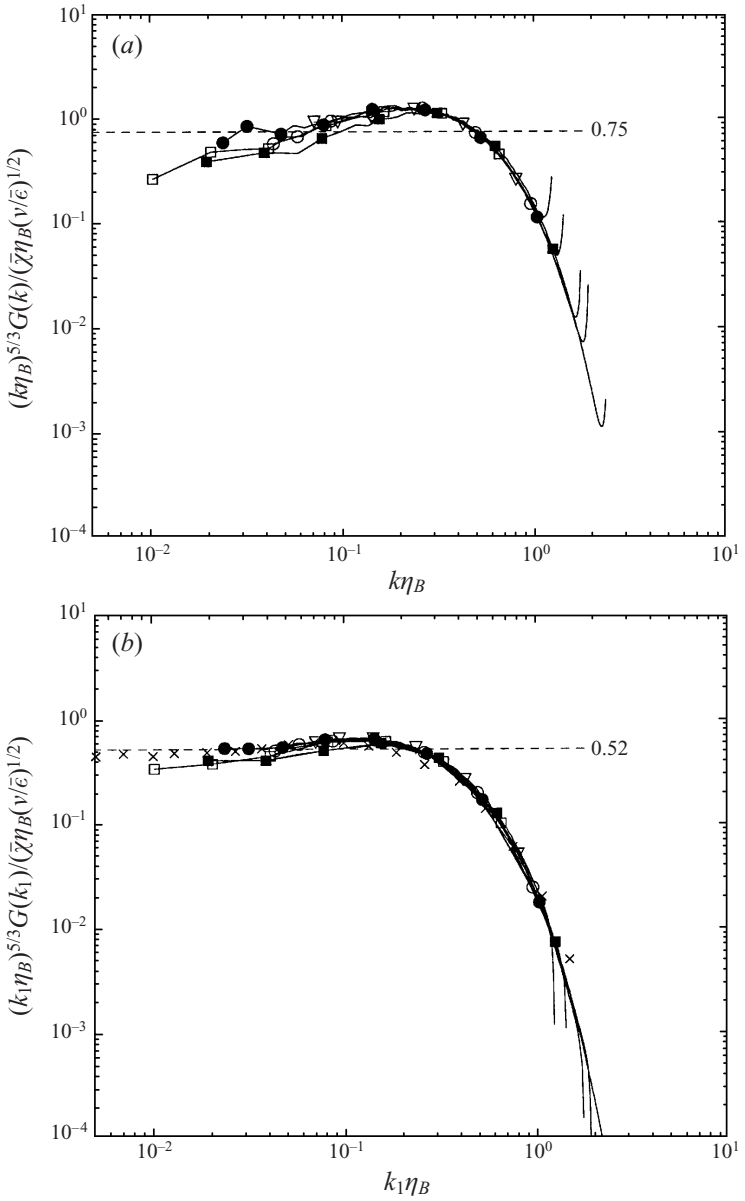

FIGURE 1. (*a*) The three-dimensional scalar variance spectrum function $G(k)$ and (*b*) the one-dimensional longitudinal scalar variance spectrum $G(k_1)$ for the simulated scalar fields shown in table 1, using Batchelor scaling. For the forced turbulence fields, only the spectra for the unforced region $k > 2$ or $k_1 > 2$ are shown. The horizontal dashed line in (*b*) marks the level of 0.52, the average Obukhov–Corrsin constant observed in experiments. □, 256^3, free-decaying flow at $R_\lambda = 132$ and $Pr = 0.7$; ■, 256^3, free-decaying flow at $R_\lambda = 68.1$ and $Pr = 0.7$; ▽, 128^3, forced stationary flow at $R_\lambda = 104$ and $Pr = 1.0$; ○, 256^3, forced stationary flow at $R_\lambda = 151$ and $Pr = 1.0$; ●, 512^3, forced stationary flow at $R_\lambda = 195$ and $Pr = 1.0$. The one-dimensional temperature spectrum of Williams & Paulson (1977) for atmospheric surface layer flow at $R_\lambda \approx 2000$ is shown by the crosses (×). These symbols are used consistently throughout the paper and are shown in table 1.

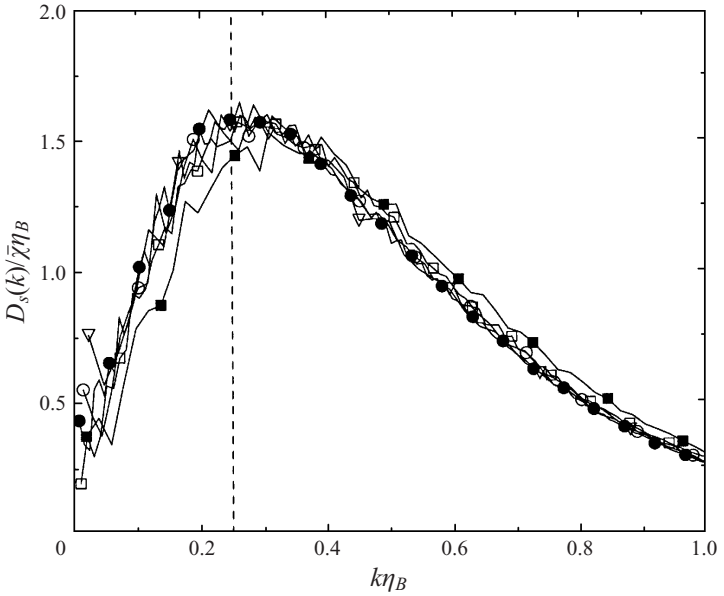

FIGURE 2. The normalized scalar dissipation spectrum. The vertical line mark the peak location at $k\eta_B = 0.25$.

which are smoother than figure 1(*a*) at low wavenumbers due to the increased sampling and the averaging over the three coordinate directions. The inertial range becomes more evident for the f512 scalar field, with a level of $C_s(1D) = 0.52$ for $k_1\eta_B < 0.05$. This corresponds to a three-dimensional Obukhov–Corrsin constant of $C_s(3D) = C_s(1D) \times \frac{5}{3} = 0.87$ (Note that the conversion relationship from $C_s(1D)$ to $C_s(3D)$ requires isotropy of the computed spectra at low wavenumbers which may not be rigorously satisfied by the simulated flow fields, e.g. Yeung & Zhou 1997.). The analyses of Hill (1978) yielded $C_s(3D) = 0.68 \sim 0.83$, while the RNG theory (Yakhot & Orszag 1986) predicts $C_s(3D) = 1.16$. DNS of Pumir (1994) give $C_s(3D) = 1.1$ and show a Pr dependence. Surveys of previous experimental data show that $C_s(1D)$ can vary from 0.31 to 1.16 (Hill 1978; Antonia, Chambers & Browne 1983; Sreenivasan 1996), with an average of about 0.40 according to the most recent survey by Sreenivasan (1996). Our value of $C_s(1D)$ compares well with the high-Péclet-number grid turbulence data of Mydlarski & Warhaft (1998) who found that $C_s(1D)$ is in the range of 0.45 to 0.55. Similar to the velocity field, the diffusive cut-off for the one-dimensional spectrum appears earlier than the three-dimensional spectrum. The bump near the dissipation peak, although less severe than in the three-dimensional spectrum, can also be observed. Also shown with crosses ($\times$) is the one-dimensional spectrum of temperature fluctuations by Williams & Paulson (1977) (taken directly from Hill 1978) for the atmospheric boundary layer at $R_\lambda \approx 2000$. The simulation data agree well with the experimental data.

Linear-linear plots for the normalized scalar dissipation rate spectra are shown in figure 2 for $k\eta_B < 1$. The data collapse well for the four fields with $R_\lambda > 100$, indicating that the Batchelor scaling (1.2) works well for moderately high Reynolds numbers. The normalized dissipation rate spectrum has a peak value of about 1.56 at $k\eta_B \approx 0.25$. This peak location also occurs at a higher wavenumber (smaller length scale) than that of energy dissipation peak which takes place at $k\eta = 0.16$ (see Part 1),

namely the smallest length scale in the scalar field is a factor 0.64 smaller for $Pr = 1$. This is also an indication that the scalar field is more intermittent than the velocity field. As R_λ decreases below 100, the normalized spectrum shifts to higher $k\eta$ and the peak magnitude decreases. Warhaft & Lumley (1978) measured both dissipation spectra in heated grid turbulence of air. They found that the energy dissipation peak occurs at $k\eta \approx 0.18$ while the temperature dissipation peak occurs at $k\eta \approx 0.25 \sim 0.27$ (or equivalently $k\eta_B \approx 0.30 \sim 0.32$). Note that $R_\lambda \approx 48$ in their experiment and the peak locations might depend on the initial grid configuration. Therefore, there is a good qualitative agreement between our DNS and their experiment.

The simulated small-scale scalar fields are nearly isotropic as demonstrated by the ratios of local scalar gradient fluctuations in different directions in table 1. Also shown in the table are a measure of scalar dissipation intermittency, $(\overline{\xi^2})^{1/2}/\overline{\chi}$, and the skewness and flatness of the dissipation fluctuations. These values show again that the scalar fields are more intermittent than the velocity fields (see table 1 in Part 1 for a comparison with the energy dissipation statistics).

Interestingly, we note that the scalar field f512 appears to be less intermittent than the f256 field (e.g. by comparing the flatnesses of the scalar derivative and scalar dissipation rate), although the former is at a higher flow Reynolds number. This could be due to the strong time fluctuations in the scalar field as discussed in Chen & Cao (1997) or the fact that the f512 was not run long enough to allow all the small-scale features to asymptote (see table 1 in Part 1 for comparison of the total integration times). It was much more expensive to run f512.

Comparisons of our simulated scalar fields with the experimental data of temperature fluctuations by Sreenivasan, Antonia & Danh (1977) for the inner region of a fully developed turbulent boundary layer and by Mydlarski & Warhaft (1988) for grid-generated turbulence are made in table 1. Note that the experimental flows are anisotropic. The general observation is that the high-order statistics were probably underestimated in the experiment of Sreenivasan *et al.* (1977) due to a finite probe resolution and other experimental difficulties as noted in § 1.

The last two quantities in table 1 are the normalized rate of production of scalar gradient and ratio of dimensionless enstrophy production (Part 1) to the dimensionless scalar gradient production. The isotropic assumption implies that (Wyngaard 1971)

$$-\overline{\frac{\partial\theta}{\partial x_i}\frac{\partial\theta}{\partial x_j}s_{ij}} = -\frac{15}{2}\overline{\left(\frac{\partial\theta}{\partial x_1}\right)^2\frac{\partial u_1}{\partial x_1}}. \tag{2.5}$$

It follows then that

$$-\overline{\frac{\partial\theta}{\partial x_i}\frac{\partial\theta}{\partial x_j}s_{ij}} = -\frac{\sqrt{30}}{6}S_m = -0.913S_m, \tag{2.6}$$

where S_m is the mixed derivative skewness shown as the sixth item in table 1. A skewness of -0.446 to -0.490 would imply a dimensionless scalar gradient production of 0.407 to 0.447, which is in excellent agreement with the dimensionless production directly computed. This kind of consistency has not been demonstrated in physical experiments, but should serve as a way of checking the accuracy of experimental measurements of small-scale quantities. To date, the scalar-gradient production term has not been measured directly. Finally, the dimensionless enstrophy production is only about half the dimensionless scalar gradient production, indicating that the scalar gradient is better aligned with the local rate of strain than the vorticity. This is consistent with previous observation, for example, by Ashurst *et al.* (1987). A larger dimensionless production also indicates the possibility of smaller length scale in the

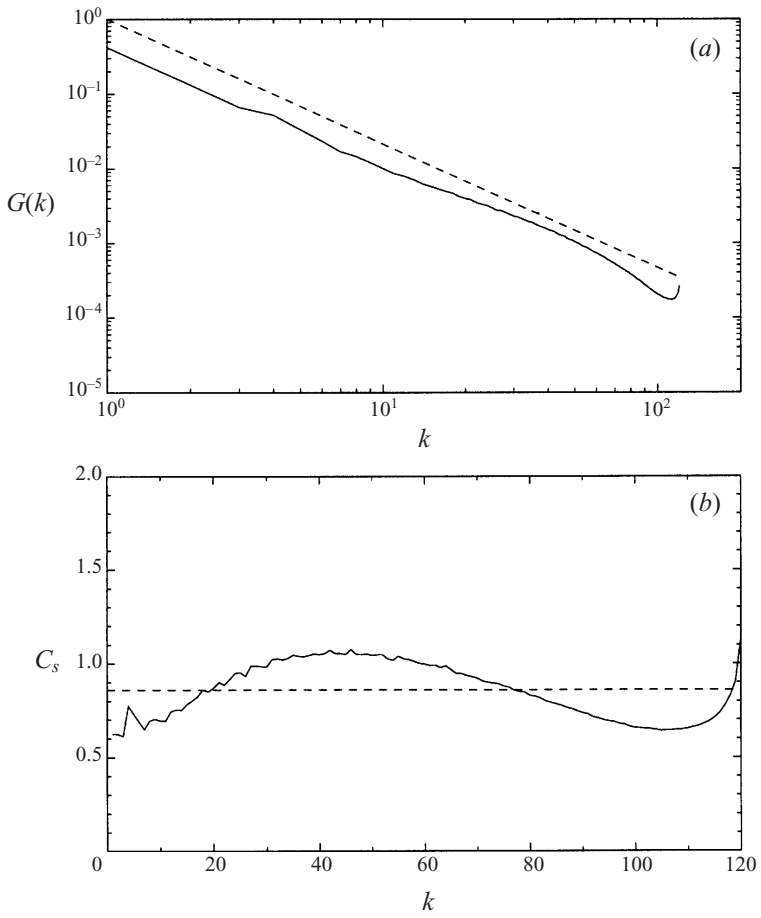

FIGURE 3. (*a*) The three-dimensional scalar variance spectrum and (*b*) the local Obukhov–Corrsin constant $C_s \equiv G(k)k^{5/3}\bar{\epsilon}^{1/3}/\bar{\chi}$ as a function of the wavenumber k for the large-eddy simulation scalar field. The dashed line in (*a*) marks the $-\frac{5}{3}$ slope. The dashed line in (*b*) marks the mean value of C_s ($C_s = 0.86$).

scalar field. It is important to note that both the dimensionless production rates and their ratio are almost independent of flow Reynolds number and large-scale forcing, which is valuable information for the modelling of turbulent scalar fields.

The scalar variance spectrum for the LES field is shown in figure 3(*a*). On the log-log plot, the spectrum has a slope around $-\frac{5}{3}$. The *local* Obukhov–Corrsin coefficient, defined as $C_s(k) = G(k)k^{5/3}\bar{\epsilon}^{1/3}/\bar{\chi}$, is plotted in figure 3(*b*) against k on a linear-linear plot. The two mean dissipation rates were estimated as the energy and scalar variance flux, respectively, from the resolved field to the subgrid scales. $C_s(k)$ varies in the range from 0.6 to 1.1, with an average value of 0.86. This value is in excellent agreement with the Obukhov–Corrsin constant obtained from DNS.

The physical space equivalence of the scalar spectrum is the second-order moment of the scalar increment as shown in figure 4, under inertial range scaling. We can clearly see a plateau region for the higher-R_λ DNS scalar fields and the LES scalar field, indicating the inertial subranges. The level of the plateau regions, H_2 in our notation, lies between 1.7 and 2.1, which, using $C_s = 0.4H_2$, gives an Obukhov–Corrsin constant of 0.68 to 0.84, in close agreement with the value obtained from the scalar

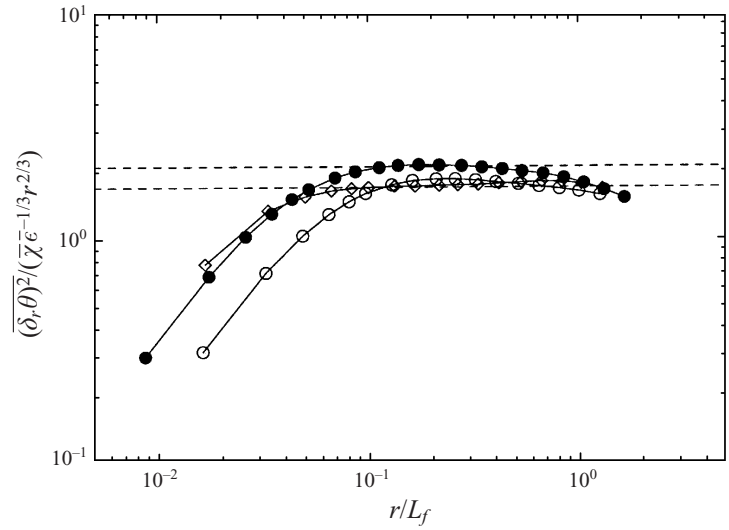

FIGURE 4. The second-order moment of the scalar increment as a function of r/L_f. The two dashed lines mark the levels 1.7 and 2.1, respectively.

spectra. A survey of early measurements shows that H_2 is in the range of 1.1 to 5.8 (Monin & Yaglom 1975). More recent experimental data of Zhu *et al.* (1995) showed that H_2 is in the range of 3.4 to 4, significantly larger than the level in our simulations. On the other hand, the high Péclet number grid turbulence data of Mydlarski & Warhaft (1998) shows $H_2 \approx 2.0$, a value very close to our observation.

Another comparison with experimental observation is displayed in figure 5, which shows the probability density function of scalar increment at small separation. The departure from Gaussianity and the existence of stretched tails are well known. Our data of different types of flows show a high degree of collapse. For the DNS fields, the p.d.f. is essentially that of scalar gradient since the scalar field is well resolved. The agreement between the DNS data and the experimental data of Antonia *et al.* (1984) and Mydlarski & Warhaft (1998) is good. We may also compare these data with the experimental data of Prasad & Sreenivasan (1990), who measured scalar (dye in water) increments at $r \approx 3\eta \approx 120\eta_B$ in a jet and wake of high Schmidt number at 1900. They only show the p.d.f. data for the region of $-4 < \Delta_r\theta/[(\Delta_r\theta)^2]^{1/2} < 4$ with $\log_{10}(\text{p.d.f.}) = -2.5$ at $|\Delta_r\theta/[\overline{(\Delta_r\theta)^2}]^{1/2}| = 4$, which compares well with our value of -2.4. The p.d.f.s also compare very well with the data of Zhu *et al.* (1995) (figure 2 in their paper).

As the separation r increases, the tails of the p.d.f. of $\Delta_r\theta$ start to drop off first while the centre region remains exponential (figure 6*a*). For r on the order of the flow integral length, the p.d.f. becomes Gaussian (figure 6*b*). This is expected since the scalar values at two points are only weakly correlated and the scalar variable itself is nearly Gaussian. Similar observations were made, for example, by Zhu *et al.* (1995) and Mydlarski & Warhaft (1998).

In summary, we have demonstrated that the simulated scalar fields have many similar characteristics known previously. In general, we find that the scalar field is more intermittent than the velocity field. We also provide a few new statistics and their scalings. Other important statistics of the highest-R_λ DNS scalar field, such as flatness factor of $\Delta_r\theta$ and the third-order mixed moment $\overline{\Delta_r u(\Delta_r\theta)^2}$, were documented by Chen & Cao (1997). They also found that the scaling exponents of the unconditioned

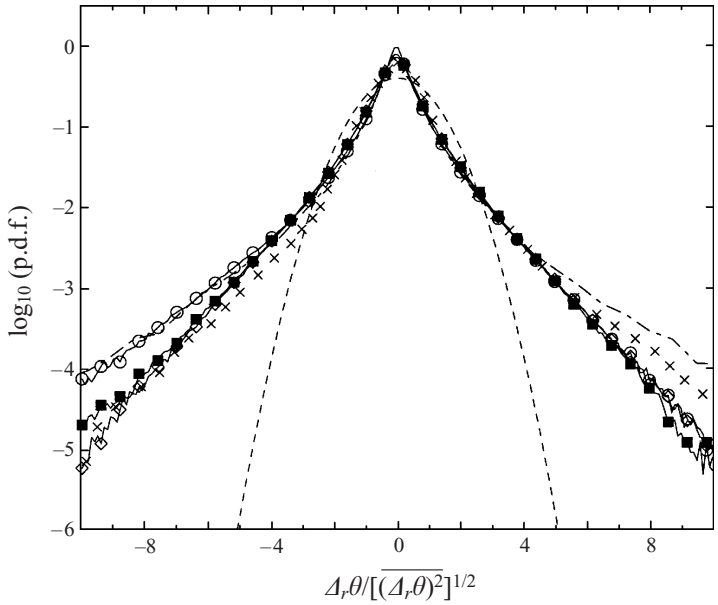

FIGURE 5. The probability density function of scalar increment at small separations. Only three simulations at 256^3 are shown with symbols following the convention given in table 1, the symbols only mark every 6 points of the DNS data for identification purpose. The separation was set to one grid spacing in the simulations. The experimental data of Antonia *et al.* (1984) for the scalar field in a round jet with $R_\lambda = 850$ are shown by the $\times$ symbols. The p.d.f. of scalar gradient for grid turbulence at $R_\lambda = 247$ and $Pr = 0.707$ (Mydlarski & Warhaft 1998) is shown by a dot-dashed line. The separation as determined by the probe resolution in their experiment was about 20η.

scalar structure function over r agree very well with the experimental data by Antonia *et al.* (1984). It is surprising that certain features of the scalar turbulence are rather insensitive to changes of global Reynolds number. This indicates that a careful study of scalar turbulence at moderate R_λ in DNS can be very relevant to high-Reynolds-number scalar turbulence.

3. Phenomenology and statistics of dissipation rate fluctuations

The statistics of locally volume-averaged kinetic energy dissipation rate were studied in Part 1. Here we focus on the statistics of the scalar dissipation rate and the correlation between the energy dissipation rate and the scalar dissipation rate. These statistics represent an important part of the refined turbulence theory for passive scalar fields.

Figure 7 shows the local scalar dissipation rate χ on a line of length $4L_f$ for three representative fields at different R_λ, where F_s^Δ in figure 7(c) for the LES field is defined as

$$F_s^\Delta \equiv 2D_t \frac{\partial\tilde{\theta}}{\partial x_i}\frac{\partial\tilde{\theta}}{\partial x_i}. \tag{3.1}$$

Here $\tilde{\theta}$ is the resolved scalar field and D_t is eddy diffusivity. F_s^Δ represents approximately the local scalar variance flux from resolved to subgrid scales. In equilibrium turbulence, this flux into the subgrid volume Δ^3 is dissipated within that volume on average. Consequently we view F_s^Δ as a good approximation for the average scalar

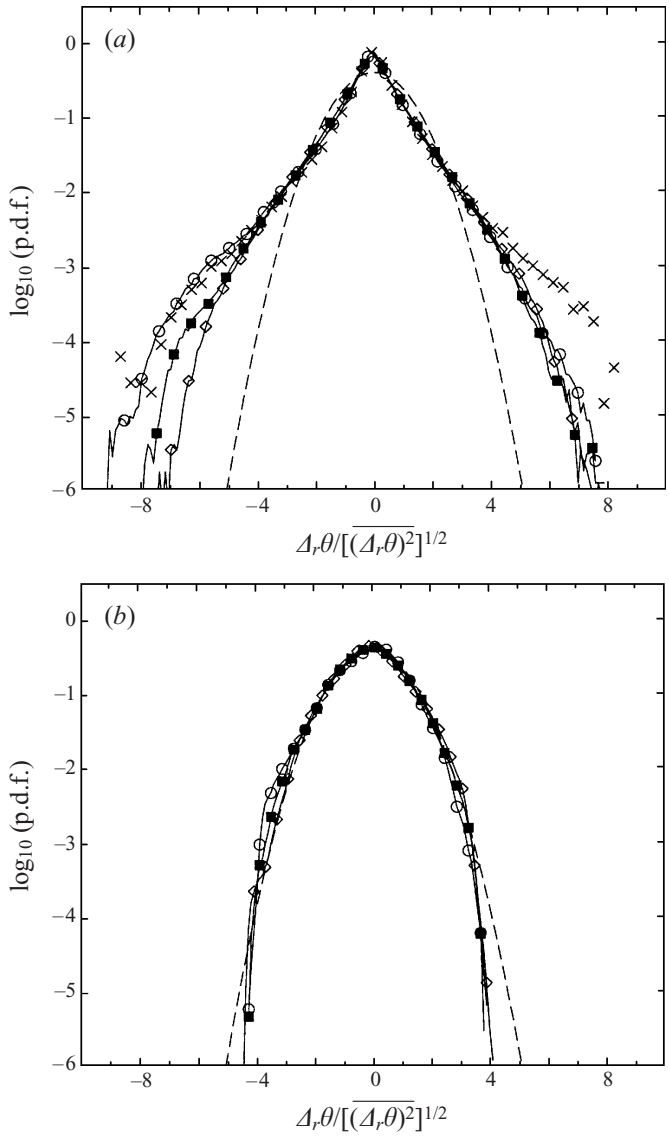

FIGURE 6. The probability density function of scalar increment at (*a*) $r = 6\Delta$ and (*b*) $r = 62\Delta$. Only three simulations at 256^3 are shown with symbols following the convention given in table 1, the symbols only mark every 6 points in (*a*) or 4 points in (*b*) of the DNS data for identification purpose. The experimental data of Mydlarski & Warhaft (1998) for grid-generated scalar turbulence with $r/\eta = 40.5$ at $R_\lambda = 247$ and $Pr = 0.707$ are shown by the $\times$ symbols. The dashed line is the Gaussian distribution.

dissipation rate in the subgrid-scale volume, i.e.

$$\chi_r(\boldsymbol{x}, t)|_{r=\Delta} \approx F_s^{\Delta}(\boldsymbol{x}, t). \tag{3.2}$$

Averages of $\chi_r(\boldsymbol{x}, t)|_{r=\Delta}$ on a linear dimension $r > \Delta$ are taken as χ_r in later scaling analyses using the LES field. This same concept was used in Part 1 to define ϵ_r for the LES field. Relative to the DNS local scalar dissipation rate χ, F_s^{Δ} in figure 7(*c*) can be viewed as local scalar dissipation rate at a much higher *effective* Reynolds

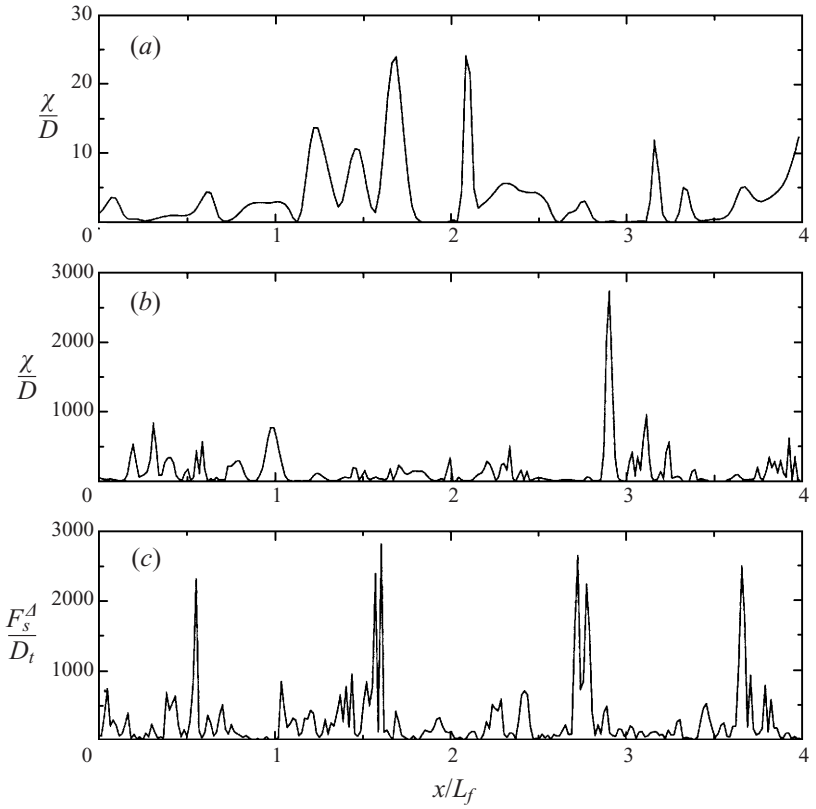

FIGURE 7. The local scalar dissipation rate or scalar flux (for the LES field only) on a line $y = z = L_B/2$ of length 4 integral length scales in the simulation box. (*a*) d256c2, $R_\lambda = 68$ and $Pr = 0.7$; (*b*) f256, $R_\lambda = 151$ and $Pr = 1.0$; and (*c*) LES256.

number averaged over grid scale Δ. Visually, the local dissipation rate becomes more spiky as R_λ increases, and both the spike magnitude and the number of spikes in one integral length scale grow with R_λ. Compared with figure 5 in Part 1, the scalar dissipation rate is much more intermittent than the local energy dissipation rate. A similar observation was made in experimental measurements by Meneveau *et al.* (1990) through local signals of pseudo-dissipation rates χ' and ϵ'.

We shall now study the locally volume-averaged scalar dissipation rate χ_r. The method for computing χ_r is identical to that used for ϵ_r (see Part 1). Figure 8 gives the probability distribution of $\ln \chi_r$ at four different r for forced turbulence f256 at $R_\lambda = 151$. Here $\ln \chi_r$ is centred on its mean $b_r \equiv \overline{\ln \chi_r}$ and normalized by its standard deviation $\pi_r \equiv \sqrt{\overline{(\ln \chi_r - b_r)^2}}$. For convenience, we define $q_r \equiv (\ln \chi_r - b_r)/\pi_r$. Also shown is the standard Gaussian distribution for comparison. Figure 8 shows that whereas $\ln \chi_r$ is nearly Gaussian for $|q_r| \leqslant 2$, the tails deviate significantly from the Gaussian distribution. Furthermore, $\ln \chi_r$ is negatively skewed at all r. These deviations from Gaussianity are greatest at small r, and appear to reduce as r increases. These observations are in good agreement with the findings of Sreenivasan *et al.* (1977) and Eswaran & Pope (1988*b*). The probability distributions of $\ln \chi_r$ for other DNS fields and the LES field are similar. We find that the skewness of $\ln \chi_r$ lies in the range -0.10 to -0.20 for small r and approaches zero as $r \to L_f$, while the flatness of

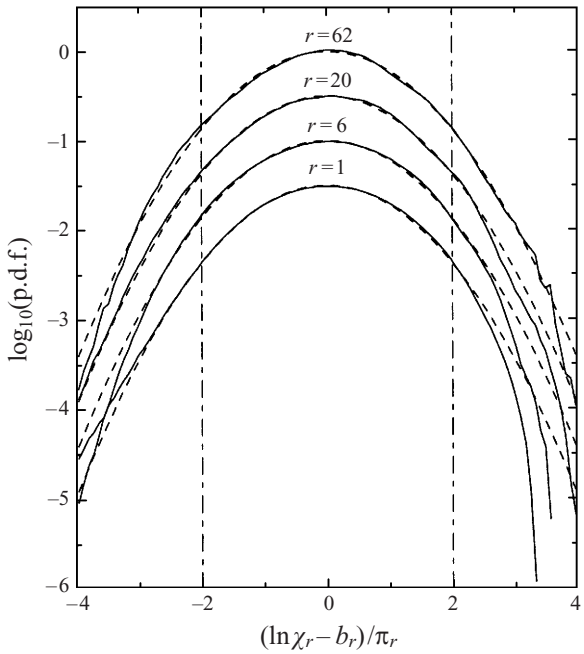

FIGURE 8. Probability density function for $\ln \chi_r$ at four different r of 1, 6, 20, 62 grid spacings for the forced DNS field at $R_\lambda = 151$ and $Pr = 1$. The curves are shifted by different amounts for $r > \Delta$. The dashed lines represent the normal distribution.

$\ln \chi_r$ is in the range 2.8 to 3.1, close to 3 for the Gaussian distribution. These values conform well with experimental data of Sreenivasan *et al.* (1977).

More detailed comparisons with the log-normal distribution can be made by computing moments of $\overline{\chi_r^n}$. For a log-normal distribution (Kolmogorov 1962),

$$\overline{\chi_r^n} = \exp(nb_r + n^2\pi_r^2/2). \tag{3.3}$$

Using $\overline{\chi_r} = \overline{\chi}$ yields for $n = 1$,

$$Q \equiv \frac{b_r + 0.5\pi_r^2}{\ln \overline{\chi}} = 1, \tag{3.4}$$

implying that the mean and standard deviation of $\ln \chi_r$ are directly related if the distribution of χ_r is log-normal. Figure 9 shows Q as a function of r. Excluding the lowest-R_λ d256c2 field, Q deviates by less than 3% from log-normality at all r, and improves with increasing r, suggesting that the log-normal model is accurate for the first-order moment $n = 1$. However, the departures from the log-normal distribution become more important for higher-order moments. To see this, we plot the non-dimensional ratio

$$R_n \equiv \frac{2}{n(n-1)} \times \frac{\ln \overline{\chi_r^n}/(\overline{\chi})^n}{\ln \overline{\chi_r^2}/(\overline{\chi})^2}, \tag{3.5}$$

against n in figure 10 for fixed r, where $R_n = 1$ when $n > 2$ if χ_r is precisely log-normal. Note that R_2 is defined to be 1. Overall, R_n decreases continuously with increasing n, indicating that the log-normal model tends to overpredict the magnitude of high-order moments, as known previously (e.g. Antonia *et al.* 1984). The departure from log-

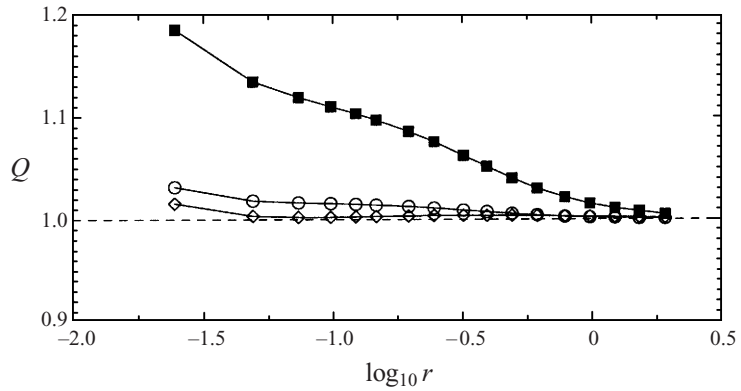

FIGURE 9. The ratio $Q \equiv (m_r + 0.5\sigma_r^2)/\ln \overline{\chi}$ for the three different types of flow fields: ■, 256^3, free-decaying flow at $R_\lambda = 68.1$ and $Pr = 0.7$; ○, 256^3, forced stationary flow at $R_\lambda = 151$ and $Pr = 1.0$; ◇, 256^3, large-eddy simulation.

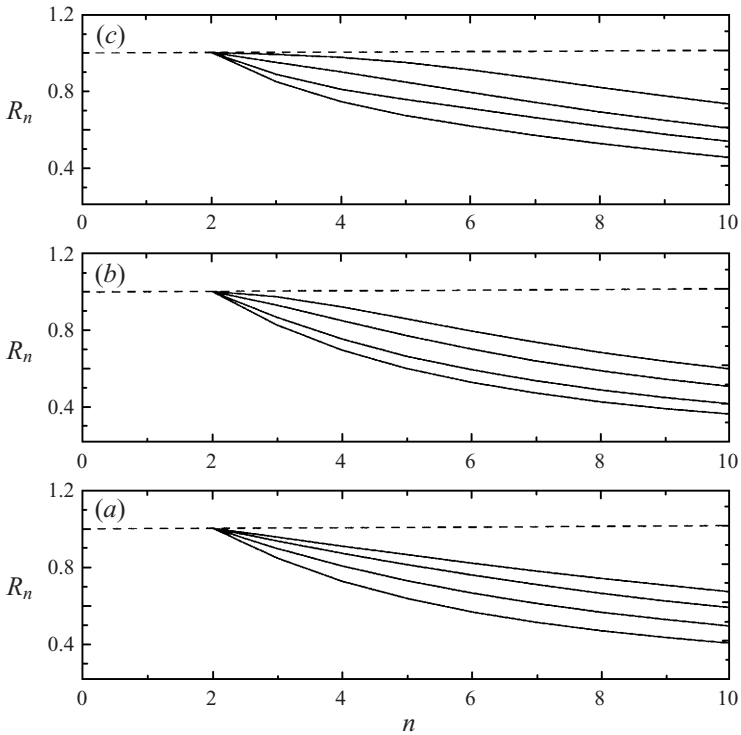

FIGURE 10. The non-dimensional ratio defined by (3.5) for the three different flow fields. The four lines in each plot, from bottom to top, are for $r = \Delta$, 6Δ, 20Δ, 62Δ, respectively. (*a*) d256c2, $R_\lambda = 68$ and $Pr = 0.7$; (*b*) f256, $R_\lambda = 151$ and $Pr = 1.0$; and (*c*) LES256 and $Pr = 1.0$.

normality decreases as r increases and approaches inertial-range scales. Furthermore, the departure is less for higher flow Reynolds number.

The dependence of the variance of $\ln \chi_r$ on r is shown in figure 11 on a linear-log plot to determine the value of μ_s in equation (1.10). The LES field displays a well-defined linear region with a slope of approximately $\mu_s = 0.43$. The DNS fields, on the other hand, display less clear linear regions at intermediate r with an approximate

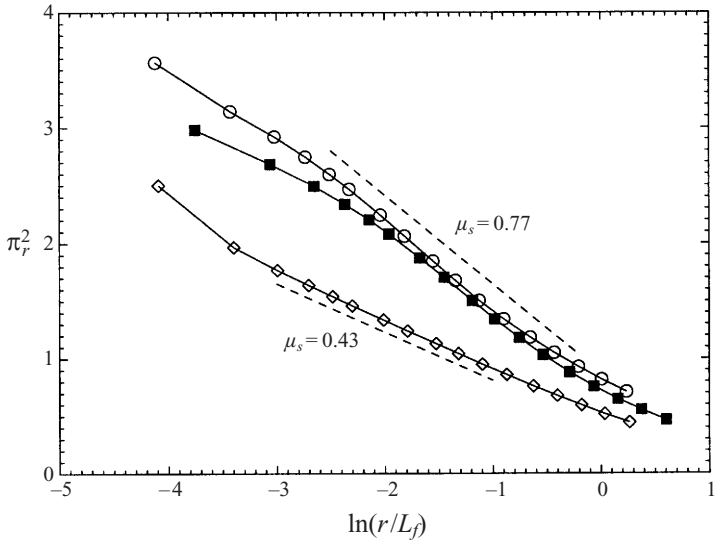

FIGURE 11. The scaling for the variance of $\ln \chi_r$: ■, 256^3, free-decaying flow at $R_\lambda = 68.1$ and $Pr = 0.7$; ○, 256^3, forced stationary flow at $R_\lambda = 151$ and $Pr = 1.0$; ◇, 256^3, large-eddy simulation.

slope $\mu_s = 0.77$. Taking the case f256, the range of r for which the slope applies is from $r/\eta = 8$ to $r/\eta = 65$ (or $r/L_f = 0.08$ to $r/L_f = 0.65$). These values of μ_s are much larger than μ for the energy dissipation rate ($\mu = 0.2$ to 0.28, Part 1). The difference between μ_s and μ appears to be consistent with the observed difference in the level of intermittency between the scalar and energy dissipations. Sreenivasan *et al.* (1977) measured the variance of $\ln \chi_r$ directly (one of the very few experiments of this kind). They found that $\mu_s = 0.35$ and that the scaling range started from $r/\eta = 6 \sim 8$. A survey by Sreenivasan *et al.* (1977) showed a range of μ_s from 0.35 to 0.72. A more recent review by Sreenivasan & Antonia (1997) indicates that the best estimate for μ_s is about 0.35 while the best estimate for μ is 0.25.

The more commonly used method for estimating μ_s experimentally is through the correlation of χ, namely $\overline{\chi(\boldsymbol{x}, t)\,\chi(\boldsymbol{x}+\boldsymbol{r}, t)} \sim r^{-\mu_s^c}$. In figure 12 we show this correlation as a function of r. The scaling is not as good as seen for the variance in figure 11. There appears to be a linear region for the LES field with $\mu_s^c = 0.27$, a value significantly less than $\mu_s = 0.43$ based on the variance method above. Note that there is no rigorous relationship between μ_s and μ_s^c. Our results seem to explain the reason for different values of μ_s (and μ) found in experiments. The review by Sreenivasan & Antonia (1997) does show that the correlation method yields a significantly smaller value of the scalar intermittency parameter than the variance method. Apart from the possible Reynolds number dependence and flow-type dependence, the dependence of the scalar intermittency parameter on measurement methods needs further study.

Having discussed the scalar dissipation rate χ_r here and the energy dissipation rate ϵ_r previously in Part 1, we shall now report on the correlation between the two. First we show in figure 13 the correlation coefficient between $\ln \epsilon_r$ and $\ln \chi_r$ as a function of r. A significant positive correlation is seen for all values of r. The general behaviour is that the correlation increases with r, reaches a maximum at a scale between η and L_f, then drops again at large r. The high-R_λ fields and the LES field show a plateau region at 0.25. Antonia & Chambers (1980) found that $\rho' \equiv \rho(\ln \chi_r', \ln \epsilon_r')$ increases from 0.40 to 0.54 in the inertial subrange in the atmospheric surface layer.

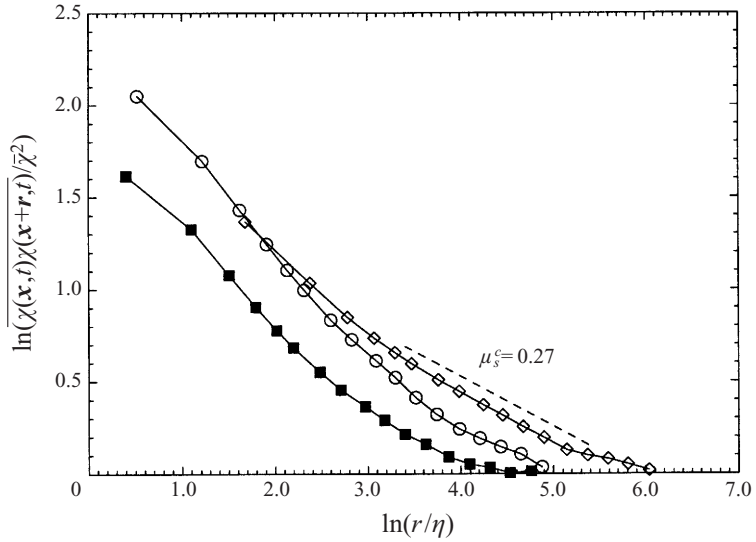

FIGURE 12. The spatial correlation coefficient of $\chi(\boldsymbol{x}, t)$ as a function of r. The dashed line marks a slope of 0.27.

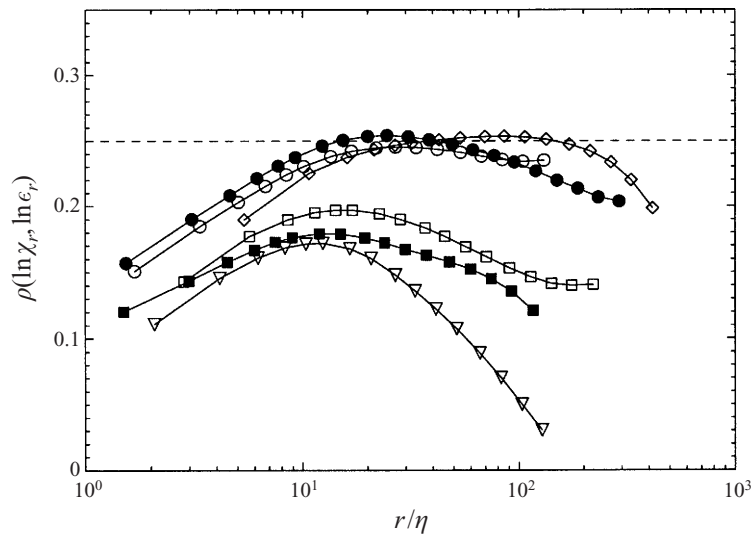

FIGURE 13. The correlation coefficient between $\ln \epsilon_r$ and $\ln \chi_r$ as a function of r/η. The line marks the level 0.25.

The theory of Hosokawa (1991) gives 0.51. Meneveau *et al.* (1990), on the other hand, found a much lower value of 0.13 ± 0.04 in the wake of a heated jet. Antonia & Chambers (1980) and Zhu *et al.* (1995) found experimentally that ρ' increases from 0.13 to 0.55 as r increases for both jet flow and the atmospheric surface layer. Note that all the experiments used pseudo-dissipation rates instead of the true dissipations. It is possible that this correlation coefficient increases with flow Reynolds number. It is also possible that the larger value observed in some experiments is due to the contamination of the passive scalar signal by velocity signals.

Finally, we show the correlation coefficient between χ_r and ϵ_r in figure 14. The

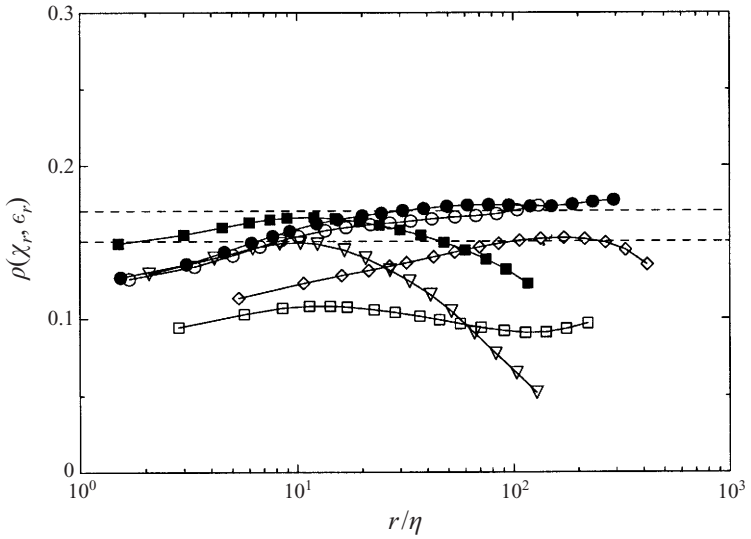

FIGURE 14. The correlation coefficient between χ_r and ϵ_r as a function of r/η. The horizontal lines mark 0.15 and 0.17.

general behaviour is similar, but the level-off in the inertial subranges is less evident. The correlation is around 0.15 to 0.17 for the high-R_λ fields and the LES field in the inertial subrange, considerably lower than $\rho(\ln\chi_r, \ln\epsilon_r)$. This difference was also noted in the measurements of Antonia & Chambers (1980). Mydlarski & Warhaft (1998) obtained a correlation coefficient of $0.13 \sim 0.14$ between the pseudo-dissipation rates χ_r' and ϵ_r' in the inertial subrange.

We have also compared the joint p.d.f.s of the logarithmic dissipation rates with the joint log-normal model, equation (1.8), by two-dimensional contour level plots of the joint p.d.f. (not shown here). We observe that the joint log-normal model is a very good model for most of the (χ_r, ϵ_r) region. The log-normal model does not fit well to the region of very large χ_r but moderate ϵ_r. The model works better for larger r and larger R_λ.

4. Direct examination of RSHP

A rather thorough examination of RSHP can now be provided. The objective is to quantify the scaling exponents of $\delta_r\theta|_{\epsilon_r,\chi_r}$ over χ_r, ϵ_r, and r, respectively. We shall denote these exponents as ϕ, α, and ζ. To compute the conditional scalar increments, $\overline{\delta_r\theta|_{\epsilon_r,\chi_r}}$, the following procedure was used: (i) for a given r, compute the value of (χ_r, ϵ_r) at each grid point; (ii) divide the dissipation-rate pair (χ_r, ϵ_r) into two-dimensional bins based on a logarithmic scale, i.e. 101 by 101 equally-spaced bins are used for the domain

$$-4 < q_r \equiv \frac{\ln\chi_r - b_r}{\pi_r} < +4, \quad -4 < s_r \equiv \frac{\ln\epsilon_r - m_r}{\sigma_r} < +4; \tag{4.1}$$

and (iii) compute $\overline{\delta_r\theta|_{\epsilon_r,\chi_r}}$ based on all the grid points falling into a particular (χ_r, ϵ_r) bin. This procedure produced a two-dimensional field for $\overline{\delta_r\theta|_{\epsilon_r,\chi_r}}$ of dimension 101×101. The computation was repeated over roughly logarithmically distributed values of r, with $r_{i+1} \approx 1.25 r_i$, starting from $r_1 = \Delta$, the grid spacing.

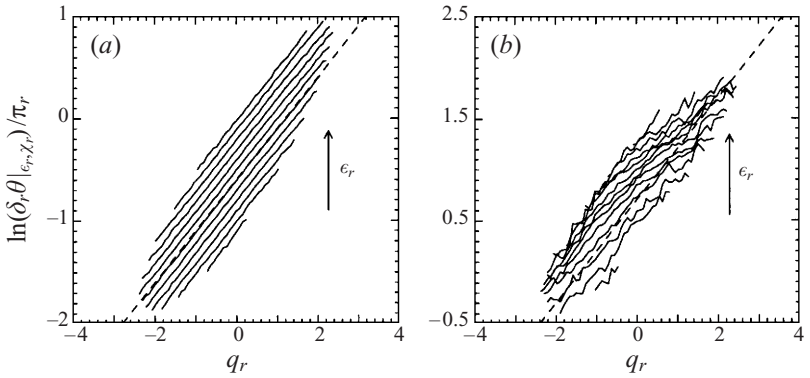

FIGURE 15. Scalar increment conditioned on the locally averaged dissipation rates, $\delta_r\theta|_{\epsilon_r,\chi_r}$, against χ_r on a log-log plot, for the 256^3 forced DNS field f256 at $R_\lambda = 151$ and $Pr = 1$. Each curve corresponds to a fixed r and ϵ_r. (*a*) $r = \Delta$; (*b*) $r = 50\Delta$. The dashed line shows $\frac{1}{2}$ slope, $q_r \equiv (\ln\chi_r - a_r)/\pi_r$.

4.1. *Scaling exponent of* $\overline{\delta_r\theta|_{\epsilon_r,\chi_r}}$ *on* χ_r

We first examine the scaling exponent of χ_r for the conditionally averaged scalar increments. For this purpose, log-log plots of $\ln(\overline{\delta_r\theta|_{\epsilon_r,\chi_r}})/\pi_r$ against q_r are presented in figure 15(*a*) for $r = \Delta$ and figure 15(*b*) for $r = 50\Delta$ for the forced DNS field f256. Different curves represent different $\ln\epsilon_r$ bins (only the bins $1, 6, 11, \ldots$, for s_r are shown). The vertical axis is shifted by an amount proportional to the s_r bin numbr to separate the curves, as otherwise all the curves almost overlap as a result of weak dependence of $\overline{\delta_r\theta|_{\epsilon_r,\chi_r}}$ on s_r. The curves fluctuate at very small and very large values of χ_r and/or ϵ_r due to the small number of samples. To eliminate these edge fluctuations from the estimation of the scaling exponent, we only use the central portion of the curves, selected by requiring the number of samples in a bin to be larger than 1000. In addition, the number of retained points on each curve is required to be larger than 5 so that a reasonable measure of slope can be made. As a result, only about 12 curves out of 21 are shown. Figure 15 shows qualitatively that the slope, which represents the scaling exponent ϕ, is close to $\frac{1}{2}$ for both r values.

Next each curve was least-squared fit with a straight line to extract the slope. For a given r, the slope was averaged over all the s_r bins. The process was repeated for all r values and different scalar fields. The final results for the scaling exponent ϕ as a function of r/η are shown in figure 16. ϕ is $\frac{1}{2}$ for the dissipation range according to the Taylor expansion, equation (1.15). In the inertial subrange, the slope should again be $\frac{1}{2}$, if RSHP is correct. Figure 16 shows that $\phi = 0.5 \pm 0.05$ for most of the r/η region. The extent of this region also increases as R_λ increases, with the LES field being most extended. The figure also shows that as r approaches the integral scale, the scaling exponent drops below $\frac{1}{2}$. Since $\delta_r\theta|_{\epsilon_r,\chi_r}$ will no longer change with r if $r \gg L_f$, the scaling exponent will approach zero for very large r.

4.2. *Scaling exponent of* $\overline{\delta_r\theta|_{\epsilon_r,\chi_r}}$ *on* ϵ_r

Similarly, we show in figure 17 $\ln(\overline{\delta_r\theta|_{\epsilon_r,\chi_r}})/\pi_r$ as a function of s_r, for different q_r bins, at a given r. For r in the dissipation range (figure 17*a*), the curves are almost horizontal, indicating no correlation between $\overline{\delta_r\theta|_{\epsilon_r,\chi_r}}$ and ϵ_r, consistent with equation (1.15). For r in the inertial subrange, a negative correlation is clearly seen, in agreement with RSHP as shown by equation (1.13).

The scaling exponent α for all the scalar fields is shown in figure 18. This is probably

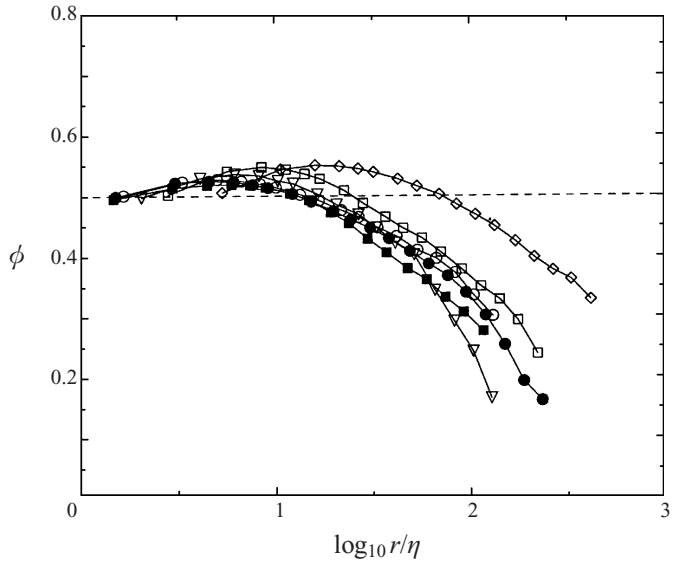

FIGURE 16. The scaling exponent of $\delta_r\theta|_{\epsilon_r,\chi_r}$ over χ_r as a function of r/η for all the DNS simulation fields. The results for the large-eddy simulation field are shown by $\diamond$, where the effective Kolmogorov scale is defined by the effective viscosity as given by equation (4.6) in Part 1.

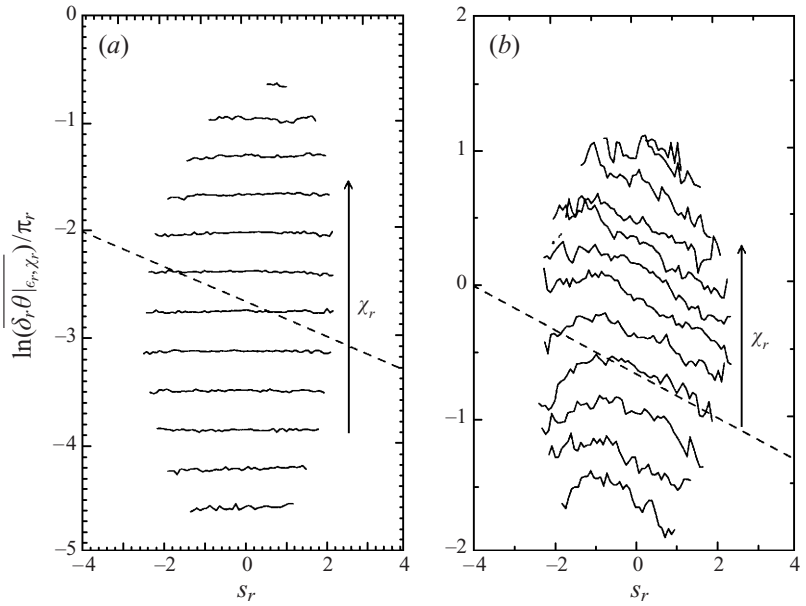

FIGURE 17. Scalar increment conditioned on the locally averaged dissipation rates, $\delta_r\theta|_{\epsilon_r,\chi_r}$, against s_r on a log-log plot, for the 256^3 forced DNS field f256 at $R_\lambda = 151$ and $Pr = 1$. Each curve corresponds to a fixed r and χ_r. (*a*) $r = \Delta$; (*b*) $r = 50\Delta$. The dashed line shows $-\frac{1}{6}$ slope. $s_r \equiv (\ln\epsilon_r - m_r)/\sigma_r$.

the most interesting figure, showing the strongest direct support for RSHP to date. The figure shows that, while there is no correlation between the conditional scalar increments and the energy dissipation rate at small r, there is a negative correlation, at larger r, between the two as signified by a negative exponent of about $-\frac{1}{6}$, in

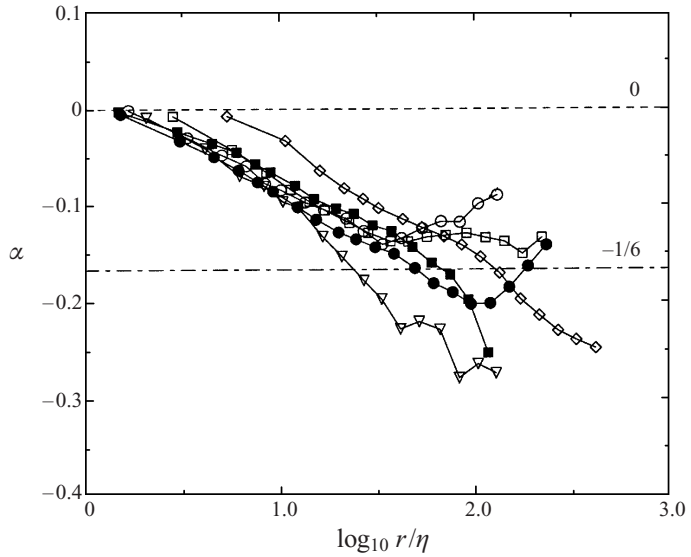

FIGURE 18. The scaling exponent of $\delta_r\theta|_{\epsilon_r,\chi_r}$ over ϵ_r as a function of r/η for all the DNS simulation fields. The results for the large-eddy simulation field are shown by $\diamond$, where the effective Kolmogorov scale is defined by the effective viscosity as given by equation (4.6) in Part 1.

good agreement with equation (1.13). The DNS fields show a good collapse of data. This negative correlation is of dynamical origin as there is no kinematic connection between the scalar increment and kinetic energy dissipation rate, while there is a kinematic connection betwen the scalar increment and scalar dissipation rate for small r, as shown by (1.15).

4.3. *Scaling exponent of* $\overline{\delta_r\theta|_{\epsilon_r,\chi_r}}$ *on* r

It is slightly more complicated to obtain the scaling exponent over r. In principle, for each bin of the fixed pair (q_r, s_r) and thus (χ_r, ϵ_r), we can plot $\overline{\delta_r\theta|_{\epsilon_r,\chi_r}}$ versus r on a log-log plot and extract the slope. Since the bin values for (χ_r, ϵ_r) depend on r, a linear interpolation procedure was used to match the value of $\overline{(\chi_r, \epsilon_r)}$ between two consecutive r values. Figure 19 gives an example of a plot for $\overline{\delta_r\theta|_{\epsilon_r,\chi_r}}$ versus r, for different χ_r bins, given $\epsilon_r \approx 0$. The curves have different slopes at small and large r, in qualitatively agreement with the theory as presented in § 1.

The local slope for each curve was obtained by finite differencing between two r fields and an average over all (χ_r, ϵ_r) bins was made to obtain ζ. The final results are given in figure 20. The exponent collapses well for different scalar fields when plotted against r/η. As expected, for small r, ζ is close to 1. As r moves to the inertial subrange, there is a strong tendency for ζ to level off at about $\frac{1}{3}$. For the LES scalar field, the $\frac{1}{3}$ range extends for almost a decade. This clearly supports the scaling dictated by RSHP.

4.4. *Dependence on* R_{ϵ_r} *and universal constants*

Since the inertial subrange is very narrow, the scaling exponents, for the most part, show a tendency of conforming with RSHP. As shown in Part 1, a better way to reveal the K62 inertial subrange is to condition on the local scale-dependent Reynolds number, $R_{\epsilon_r} = \epsilon_r^{1/3} r^{4/3}/\nu$, along the line of the first RSHP, equation (1.11). We make

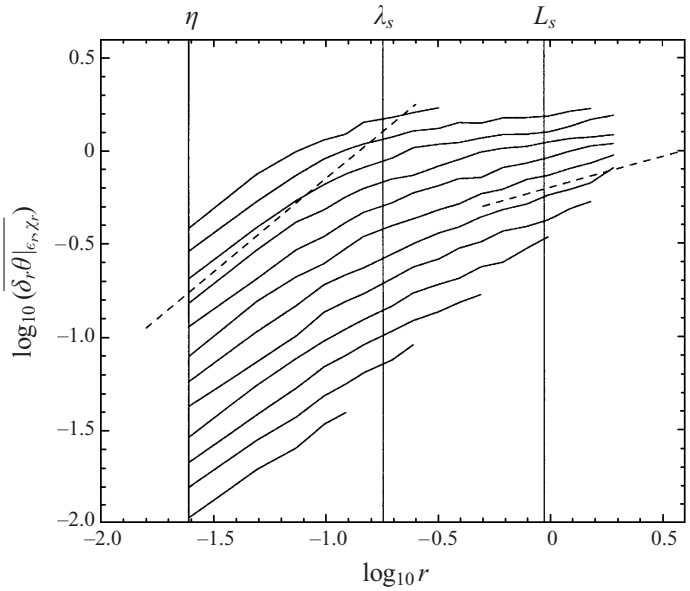

FIGURE 19. Scalar increment conditioned on the locally averaged dissipation rates, $\delta_r\theta|_{\epsilon_r,\chi_r}$, against r on a log-log plot, for the 256^3 forced DNS field f256 at $R_\lambda = 151$ and $Pr = 1$. Each curve corresponds to a fixed ϵ_r and χ_r: $\epsilon_r \approx 0$ while χ_r was varied from curve to curve, according to the binning scheme as discussed at the beginning of § 4. The dashed lines mark the $\frac{1}{2}$ and $\frac{1}{3}$ slopes.

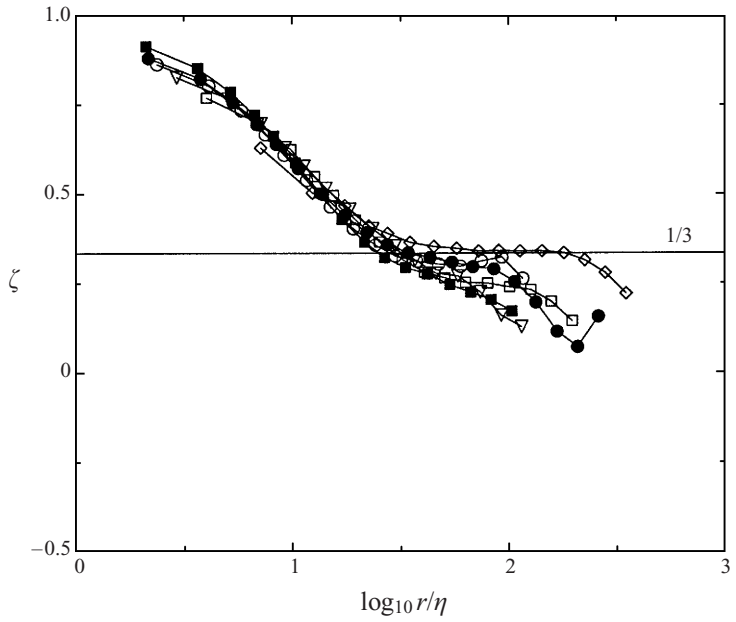

FIGURE 20. The scaling exponent of $\delta_r\theta|_{\epsilon_r,\chi_r}$ over r as a function of r/η for all the DNS simulation fields. The results for the large-eddy simulation field are shown by ◇, where the effective Kolmogorov scale is defined by the effective viscosity as given by equation (4.6) in Part 1.

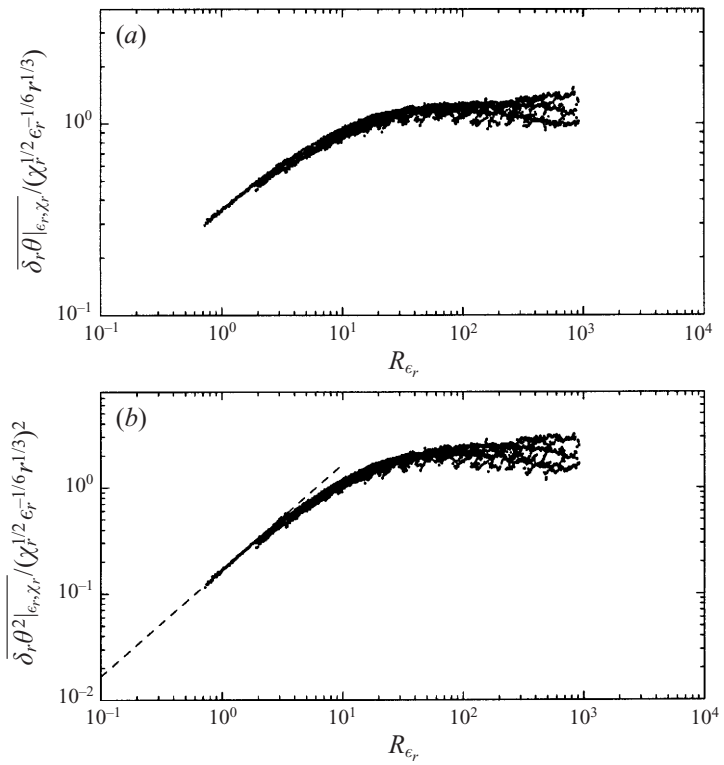

FIGURE 21. The dimensionless scalar increments against the local Reynolds number R_{ϵ_r} for the 256^3 DNS field at $R_\lambda = 151$ and $Pr = 1$. (*a*) $n = 1$; (*b*) $n = 2$, the relation $\overline{(\delta_r\theta^2|\epsilon_r, \chi_r)}/(\chi_r^{1/2}\epsilon_r^{-1/6}r^{1/3})^2 = PrR_{\epsilon_r}/6$ is shown as a dashed line.

use of the two forced DNS fields at the highest R_λ and the LES field. We first plot the first- and second-order dimensionless scalar increments as a function of R_{ϵ_r} in figure 21 for the f256 scalar field. Figure 21(*a*) is essentially a replot of figure 15 for all ϵ_r and r. A dot is drawn for each r and each bin in (q_r, s_r) if there are at least 1000 samples. Several interesting observations can be made. First, all the points collapse reasonably well in figure 21, indicating that the first RSHP, equation (1.11), provides a reasonable description for the conditionally averaged velocity increments. Second, the local Reynolds number R_{ϵ_r} extends over about three and half decades, from 0.5 to over 1000, much larger than the length-scale separation in r, which is less than two decades (e.g. figure 4). Third, based on a Taylor series expansion for $r \to 0$, for small R_{ϵ_r} the Reynolds number dependence should be

$$P_n(R_{\epsilon_r}, Pr) \propto (Pr\ R_{\epsilon_r})^{n/2}. \tag{4.2}$$

For $n = 1$ and $n = 2$, the slope should be 0.5 and 1.0, respectively, which is the case for $R_{\epsilon_r} \lesssim 20$. For $n = 2$, there is an exact relationship

$$P_2(R_{\epsilon_r}, Pr) = \frac{Pr\ R_{\epsilon_r}}{6}, \tag{4.3}$$

which agrees with the data for $R_{\epsilon_r} \lesssim 20$.

Most interestingly, those points following the inertial-subrange scaling in RSHP form plateau regions for $R_{\epsilon_r} \gtrsim 40$. This suggests that the inertial-range scaling in

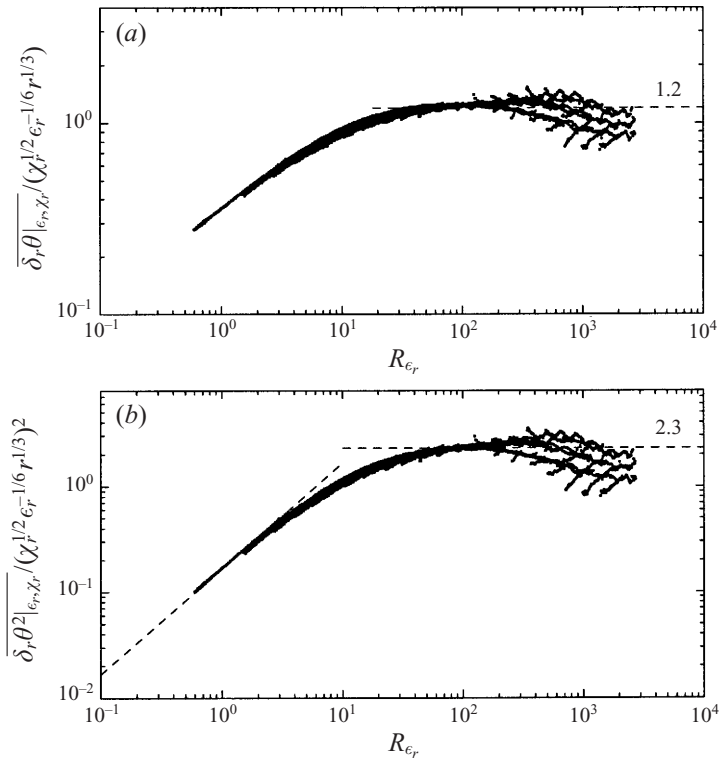

FIGURE 22. As figure 21 but for the 512^3 DNS field at $R_\lambda = 195$ and $Pr = 1$.

RSHP starts at $R_{\epsilon_r} \approx 40$. This agrees with $R_{\epsilon_r} \approx 50$ as suggested by Zhu *et al.* (1995) based on experimental data and use of pseudo-dissipation rates. The somewhat smaller value of the transition R_{ϵ_r} could be due to the use of true dissipation rates here (for a discussion of the comparison between true dissipation rate and pseudo-dissipation rate on the quality and extent of oberved scaling, see Part 1).

Figure 22 shows similar results for the f512 field. The overall features are similar to figure 21, but with a slightly wider plateau. The level of the plateau provides a reasonably accurate estimate for the universal constant W_n in equation (1.13). The estimates according to figure 22 are $W_1 = 1.2 \pm 0.1$ and $W_2 = 2.3 \pm 0.2$. Similar plots for third and fourth orders yield $W_3 = 5.5 \pm 0.5$ and $W_4 = 14.0 \pm 1.0$. Zhu *et al.* (1995) found $W_2 = 4.0 \sim 5.6$ experimentally. Three differences between our estimates and their estimates of W_n are: (i) their values are significantly larger than ours; (ii) their estimate shows a significant Reynolds number and flow type dependence while our estimate is rather insensitive to the change of flow Reynolds number, large-scale forcing, and subgrid-scale modelling; and (iii) our estimate of the universal constants for the scalar field is almost identical to that of velocity field while they show the universal constants for the scalar field are a factor of 2 larger than those of the velocity field. In Part 1, we showed that, while the use of pseudo-dissipation rates decreases the quality of the inertial-range scaling, the universal constants remain the same. We believe the experimental difficulties mentioned earlier could contribute to these differences.

To construct a similar plot using the LES field, we introduce an effective viscosity ν_e and effective diffusivity D_e. They are estimated according to field-averaged kinetic

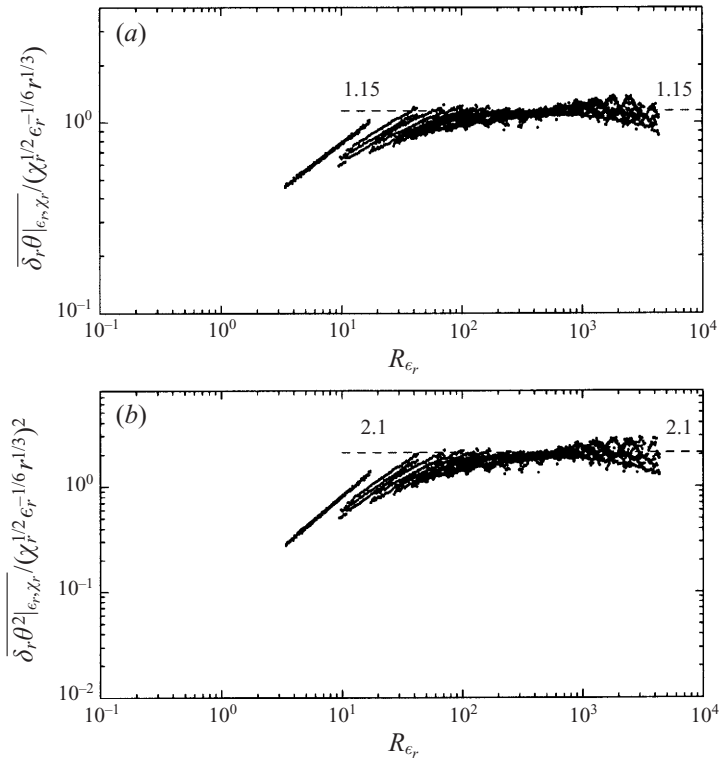

FIGURE 23. As figure 21 but for the 256^3 LES field.

energy flux and scalar variance flux as

$$v_e \equiv \frac{\overline{F^{\Delta}}}{\overline{2\tilde{s}_{ij}\tilde{s}_{ij}}}, \quad D_e \equiv \frac{\overline{F_s^{\Delta}}}{\overline{2\dfrac{\partial\tilde{\theta}}{\partial x_i}\dfrac{\partial\tilde{\theta}}{\partial x_i}}}, \tag{4.4}$$

where $\tilde{s}_{ij}$ is the rate of strain computed according to the resolved velocity field. The resulting viscosity and diffusivity are $v_e = 0.000434$ and $D_e = 0.000748$, yielding a turbulent Prandtl number of 0.58. This Prandtl number should be equal to the input Prandtl number of 0.60, on average. With these parameters, the corresponding plot for the LES field is constructed (figure 23). The plateau regions for both the first and second moments extend over a decade, giving $D_1 = 1.15 \pm 0.1$ and $D_2 = 2.1 \pm 0.2$, almost the same values as for the DNS scalar fields.

Alternatively, these universal constants can be estimated from the probability density function of β_s in the inertial subrange:

$$W_n = \int_0^{\infty} \beta_s^n f(\beta_s)\,\mathrm{d}\beta_s. \tag{4.5}$$

We computed $f(\beta_s)$ based on a small selected (ϵ_r, r) domain that forms part of the plateau regions in figures 21 to 23. Figure 24 shows the probability distributions on log-arithmic scales, along with the Gaussian curve. The probability distribution is almost the same for the three different scalar fields, supporting the universality of the distribution. The discrepancy at large β_s may be due to statistical variability. In agreement with experimental observations of Stolovitzky *et al.* (1995) and Zhu *et al.*

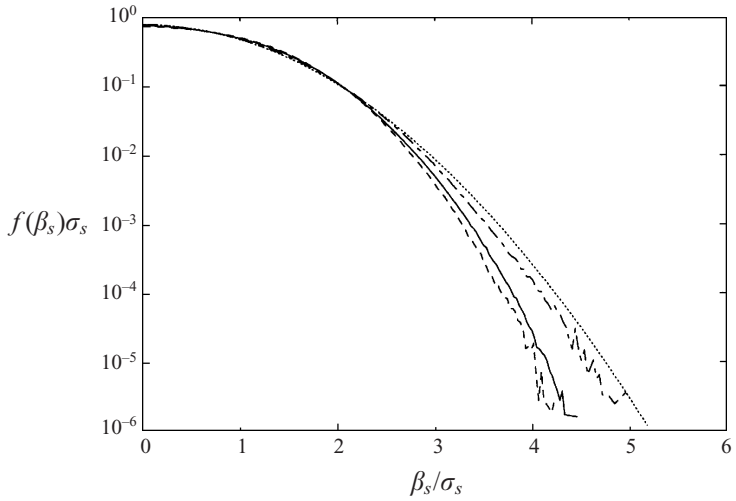

FIGURE 24. The probability distribution of β_s normalized by its standard deviation in the inertial subrange in the context of K62 on a log scale for three different flow fields: the 256^3 forced DNS flow (dashed line), the 512^3 forced DNS flow (solid line), and the LES field (chain-dotted line). The dotted line shows Gaussian distribution.

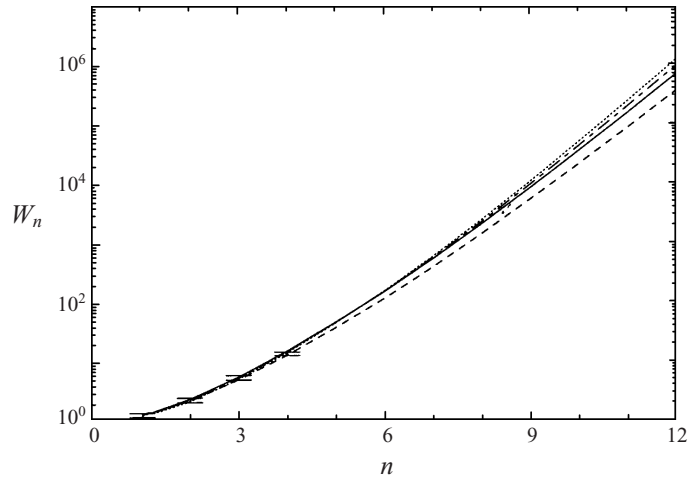

FIGURE 25. The universal constants W_n based on the probability distributions of β_s shown in figure 24 for the three different flow fields (line captions are the same as figure 24). Symbols are values determined from figures 21 to 23. The dotted line is the analytical expression based on the Gaussian model, equation (4.11) in Part 1.

(1995), the probability distribution is close to Gaussian, but falls off slightly faster than the Gaussian curve at large β_s.

The moments of β_s can be reasonably modelled by the Gaussian distribution, as shown in figure 5. The analytical result for the Gaussian model is given in Part 1 and is plotted here for comparison. The numerical value of W_n was obtained through equation (4.5) for the three fields. Also shown are the values and error bars obtained from the moments of scalar increments. They compare extremely well, indicating the probability distribution in figure 24 is reasonably accurate. It is important to note

that W_n increases with n at a *faster-than-exponential* rate. Figure 25 indicates that the Gaussian model works well, except for very large n.

5. Summary and concluding remarks

High-resolution simulations of scalar turbulence have been undertaken to study small-scale phenomenology. The main focus was to examine the refined turbulence theory when applied to passive scalar turbulence. Both aspects of the refined theory are investigated: the distribution of the locally volumed-averaged scalar dissipation rate and kinetic energy dissipation rate, and the refined similarity hypotheses for passive scalar fluctuations (RSHP). We found that the log-normal assumption provides a reasonable description, as the scale r is increased towards the inertial subrange. The correlation coefficient between the logarithmic dissipation rates is close to 0.25 and that between the dissipation fluctuations is about 0.15 to 0.17. These values are within the range of experimental observations in terms of one-dimensional surrogates of the dissipation rates. The fact that these correlation values are insensitive to flow Reynolds number, large-scale forcing, and subgrid modelling in our simulations, provided that a narrow inertial subrange exists, along with the accuracy of these statistics, makes these values representative of what would be observed for higher flow Reynolds numbers. To date, it has not been possible to experimentally measure these correlations in terms of the true dissipation rates. The intermittency parameter μ_s of the scalar dissipation fluctuations has been measured by various methods (e.g. Sreenivasan & Antonia 1997). We show that the variance method yields a much higher value than the correlation method, in agreement with the accumulated experimental evidence (Sreenivasan & Antonia 1997). An attempt to use different methods to estimate μ_s in a single experimental study needs to be made to further clarify this observed dependence of μ_s on the methods.

Various observations from our simulated scalar fields show support for RSHP: (i) for the first time, scaling exponents of the conditional scalar increments have been quantified to show a tendency to approach the K62 inertial-subrange scalings; (ii) a wider inertial subrange of the conditional statistics is observed in terms of the K62 local Reynolds number R_{ϵ_r}; (iii) the probability distribution of the random variable β_s is shown to be Gaussian and insensitive to flow Reynolds number, large-scale forcing, and subgrid modelling. The most important is the first quantitative confirmation of the $-\frac{1}{6}$ scaling of $\overline{\delta_r\theta|_{\epsilon_r,\chi_r}}$ over ϵ_r, as this shows clearly a dynamic aspect of RSHP. Note that the relationship between the velocity increments and energy dissipation rate has both kinematic and dynamic aspects (Chen, Doolen & Kraichnan 1995). The moments of β_s are different from the experimental observations of Zhu *et al.* (1995) in two ways: (i) our moments are much smaller and (ii) our moments are independent of flow Reynolds number, large-scale forcing, and subgrid modelling. The exact reason for the differences between the simulation results and experiments is not clear. Possible reasons include the use of pseudo-dissipation rates in experiments, the limited scale separation in simulations, and various experimental difficulties of measuring both dissipation rates accurately and simultaneously.

The accumulated evidence shows that while the velocity increments depend on both locally averaged dissipation rate and enstrophy at least for finite flow Reynolds number (e.g. Grossmann *et al.* 1997; Chen *et al.* 1997), the scalar increments mainly depend on the locally averaged dissipation rates. The stretching of the scalar by local velocity strain can alter quickly the local scalar gradient and thus the scalar increment. The flow vorticity could also enhance the local scalar gradient if the scalar field is

locally non-uniform (e.g. Wang & Maxey 1993). In fully developed turbulence, the vortex tubes can generate large jumps in scalar field near these tubes (Pumir 1994). The possibility of dependence of high-order scalar statistics (such as the conditional statistics of increments of scalar gradient) on local enstrophy cannot be ruled out.

A very interesting picture emerging from this work is that the small-scale features of the scalar field and those of the velocity field share both significant differences as well as similarities. Both old and new unconditional statistics show that the scalar field is more intermittent than the velocity field for $Pr \approx 1$: (i) the local signal of the scalar dissipation rate shows, within one integral length scale, a larger number of spikes with higher magnitude than that of energy dissipation rate, (ii) the flatness factors of the scalar gradient, of scalar increments over inertial-subrange scales (Chen & Cao 1997), and of the scalar dissipation-rate fluctuations are larger than those of velocity gradient, velocity increments, and energy dissipation-rate fluctuations; (iii) the scalar field has a smaller Taylor microscale; (iv) it is certain, for the given flow Reynolds numbers studied here, that the intermittency parameter μ_s of the scalar variance dissipation rate is a factor 2 larger than the intermittency parameter μ of the energy dissipation rate; (v) the length scale associated with the scalar dissipation peak is smaller than that of kinetic energy dissipation; and (vi) the dimensionless production rate of scalar gradient is a factor 2 larger than that of enstrophy. Most of these observations are not new (e.g. Sreenivasan & Antonia 1997), although we believe that these statistics may have been measured more accurately in this work than what is possible in laboratory and field experiments. The accurate evaluation of these statistics, albeit made at moderate flow Reynolds numbers, could help clarify the uncertainties surrounding the above comparisons due to experimental difficulties. For example, there is a significant overlap between the experimental values of μ and μ_s (Sreenivasan & Antonia 1997); our results support the belief that $\mu_s > \mu$. Thus the unconditional scalar field is more intermittent than the velocity field, over both dissipation and inertial-range scales. Qualitative explanations for the differences between the scalar and velocity fields exist, for example, in terms of relative alignment of the scalar gradient and vorticity with the rate-of-strain field and related structures (Kerr 1985; Ashurst *et al.* 1987; Ruetsch & Maxey 1992; Miller *et al.* 1995). Quantitative models for the above differences do not exist. The statistics provided in this paper would be useful for testing future models of this kind. It should be noted that the advection of passive scalar by a rapidly decorrelating random velocity field (Kraichnan 1974*b*; Chen & Kraichnan 1998), being a theoretically more tractable problem, has shed some light on the build-up of scalar intermittency through repeated random straining or cascades.

On the other hand, the conditional statistics along the lines of Kolmogorov refined turbulence theory show almost identical results, namely the two random variables β and β_s have a Gaussian probability distribution with *almost identical moments in the K62 inertial subrange*. This latter observation is somewhat different from experimental observations by Zhu *et al.* (1995) that the conditional moments are quite different for the velocity and scalar fields. Our results imply that the stronger intermittency of the scalar field is due to the dual dependence of the scalar field on energy and scalar dissipation rates and also the stronger intermittency of the scalar dissipation rate. The fact that the p.d.f.s of β and β_s are Gaussian implies that the strong intermittencies in the velocity and scalar fields are essentially removed as a result of the conditioning over the two dissipation fluctuations.

We focus our analyses on the scalar increments only. The scalings of conditional moments of mixed velocity and scalar increments, while in principle derivable from the scalings of first-order moments studied in this paper and Part 1, may be worth

a separate study. Experimental studies of the mixed moments have been done, for example, by Zhu *et al.* (1995).

We also limit our discussions to full dissipation rates. Some differences of using pseudo-dissipation rates for scalar field are documented, for example, by Sreenivasan *et al.* (1977). We expect the general conclusions would be similar to those indicated in Part 1 and Hosakawa & Oide (1996). Nevertheless, since experimental measurements are almost always based on the the pseudo-dissipation rates, testing the use of pseudo dissipation rates may prove to be necessary. This task would be better conducted when higher Reynolds number DNS become possible.

We thank Guowei He, Robert H. Kraichnan, Charles Meneveau, K. R. Sreenivasan, Gustavo Stolovitzky, and John Wyngaard for useful discussions. Yong Zhou provided assistance in LaTex processing and typing. L. P. W. is grateful to Raoyang Zhang for helping arrange his visit to Los Alamos during which this paper was written. This work was supported by ARO/URI grant DAAL03-92-G-0117 (monitored by Dr Walter Bach), AFOSR/URI grant number AFOSR-90-0113 (monitored by Dr James McMichael), and the US Department of Energy through Los Alamos National Laboratory. The numerical simulations were performed on the CM-5 at the Advanced Computing Laboratory at Los Alamos National Laboratory.

REFERENCES

Anselmet, E., Gagne, Y., Hopfinger, E. J. & Antonia, R. A. 1984 High-order velocity structure functions in turbulent shear flows. *J. Fluid Mech.* **140**, 63–89.

Antonia, R. A. & Chambers, A. J. 1980 On the correlation between turbulent velocity and temperature derivatives in the atmospheric surface layer. *Boundary-Layer Met.* **18**, 399–410.

Antonia, R. A., Chambers, A. J. & Browne, L. W. B. 1983 Relationship between velocity and temperature in a turbulent jet. *Exps. Fluids* **1**, 213–219.

Antonia, R. A., Hopfinger, E. J., Gagne, Y. & Anselmet, F. 1984 Temperature structure functions in turbulent shear flows. *Phys. Rev.* A **30**, 2704–2707.

Antonia, R. A. & Van Atta, C. W. 1978 Structure functions of temperature fluctuations in turbulent shear flows. *J. Fluid Mech.* **84**, 561–580.

Ashurst, W. T., Kerstein, A. R., Kerr, R. M. & Gibson, C. H. 1987 Alignment of vorticity and scalar gradient with strain in simulated Navier–Stokes turbulence. *Phys. Fluids* **30**, 3243–3253.

Batchelor, G. K. 1959 Small-scale variation of convected quantities like temperature in turbulent fluid. Part 1. General discussion and the case of small conductivity. *J. Fluid Mech.* **5**, 113–133.

Batchelor, G. K., Howells, I. D. & Townsend, A. A. 1959 Small-scale variation of convected quantities like temperature in turbulent fluid. Part 2. The case of large conductivity. *J. Fluid Mech.* **5**, 134–139.

Boratav, O. N. & Pelz, R. B. 1997 Structures and structure functions in the inerital range of turbulence. *Phys. Fluids* **9**, 1400–1415.

Camussi, R. & Benzi, R. 1997 Hierarchy of transverse structure functions. *Phys. Fluids* **9**, 257–259.

Cao, N. & Chen, S. 1997 An intermittency model for passive scalar turbulence. *Phys. Fluids* **9**, 1203–1205.

Chen, S. & Cao, N. 1997 Anomalous scaling and structure instability in three-dimensional passive scalar turbulence. *Phys. Rev. Lett.* **78**, 3459–3462.

Chen, S., Doolen, G. D., Kraichnan, R. H. & She, Z.-S. 1993 On statistical correlations between velocity increments and locally averaged dissipation in homogeneous turbulence. *Phys. Fluids* A **5**, 458–463.

Chen, S., Doolen, G. D., Kraichnan, R. H. & Wang, L. P. 1995 Is the Kolmogorov refined similarity relation dynamic or kinematic? *Phys. Rev. Lett.* **74**, 1755–1758.

Chen, S. & Kraichnan, R. H. 1998 Simulations of a randomly advected passive scalar field. *Phys. Fluids* **10**, 2867–2884.

Chen, S. & Shan, X. 1992 High resolution turbulence simulations using the Connection Machine-2. *Comput. Phys.* **6**, 643–646.

Chen, S., Sreenivasan, K. R., Nelkin, M. & Cao, N. 1997 Refined similarity hypothesis for transverse structure functions in fluid turbulence. *Phys. Rev. Lett.* **79**, 2253–2256.

Corrsin, S. 1951 On the spectrum of isotropic temperature fluctuations in isotropic turbulence. *J. Appl. Phys.* **22**, 469–473.

Dhruva, B., Tsuji, Y. & Sreenivasan, K. R. 1997 Transverse structure functions in high-Reynolds-number turbulence. *Phys. Rev.* E **56**, R4928–R4930.

Eswaran, V. & Pope, S. B. 1988*a* An examination of forcing in direct numerical simulations of turbulence. *Computers Fluids* **16**, 257–278.

Eswaran, V. & Pope, S. B. 1988*b* Direct numerical simulations of the turbulent mixing of a passive scalar. *Phys. Fluids* **31**, 506–524.

Frisch, U., Sulem, P. L. & Nelkin, M. 1978 A simple model of intermittent fully-developed turbulence. *J. Fluid Mech.* **87**, 719–736.

Grossmann, S., Lohse, D. & Reeh, A. 1997 Different intermmittency for longitudinal and transverse turbulence fluctuations. *Phys. Fluids* **9**, 3817–3825.

Hill, R. J. 1978 Models of the scalar spectrum for turbulent advection. *J. Fluid Mech.* **88**, 541–562.

Hosokawa, I. 1991 Temperature structure functions in isotropic turbulence. *Phys. Rev.* A **43**, 6735–6739.

Hosokawa, I. 1994 Probability distribution function of the temperature increment in isotropic turbulence. *Phys. Rev.* E **49**, R4775.

Hosokawa, I. & Oide, S. 1996 Isotropic turbulence: Important differences between true dissipation rate and its one-dimensional surrogate. *Phys. Rev. Lett.* **27**, 4548–4551.

Hosokawa, I. & Yamamoto, K. 1992 Evidence against the Kolmogorov refined similarity hypothesis. *Phys. Fluids* A **4**, 457–459.

Jayesh, Tong, C. & Warhaft, Z. 1994 On temperature spectra in grid turbulence. *Phys. Fluids* **6**, 306–312.

Kerr, R. T. 1985 High-order derivative correlations and the alignment of small-scale structures in isotropic numerical turbulence. *J. Fluid Mech.* **153**, 31–58.

Kerr, R. T. 1990 Velocity, scalar and transfer spectra in numerical turbulence. *J. Fluid Mech.* **211**, 309–332.

Kolmogorov, A. N. 1941*a* The local structure of turbulence in incompressible viscous fluid for very large Reynolds numbers. *C. R. Acad. Sci. URSS* **30**, 301–305.

Kolmogorov, A. N. 1941*b* Dissipation of energy in the locally isotropic turbulence. *C. R. Acad. Sci. URSS* **32**, 19–21.

Kolmogorov, A. N. 1962 A refinement of previous hypotheses concerning the local structure of turbulence in a viscous incompressible fluid at high Reynolds number. *J. Fluid Mech.* **13**, 82–85.

Kraichnan, R. H. 1974*a* On Kolmogorov's inertial-range theories. *J. Fluid Mech.* **62**, 305–330.

Kraichnan, R. H. 1974*b* Convection of a passive scalar by a quasi-uniform random straining field. *J. Fluid Mech.* **64**, 737–762.

Landau, L. E. & Lifshitz, E. M. 1959 *Fluid Mechanics.* Pergamon.

Meneveau, C. & Sreenivasan, K. R. 1991 The multifractal nature of turbulent energy dissipation. *J. Fluid Mech.* **224**, 429–484.

Meneveau, C., Sreenivasan, K. R., Kailasnath, P. & Fan, M. S. 1990 Joint multifractal measures: theory and applications to turbulence. *Phys. Rev.* A **41**, 894–913.

Métais, O. & Lesieur, M. 1992 Spectral large-eddy simulation of isotropic and stably stratified turbulence. *J. Fluid Mech.* **239**, 157–194.

Miller, R. S., Jaberi, F. A., Madnia, C. K. & Givi, P. 1995 The structure and the small-scale intermittency of passive scalars in homogeneous turbulence. *J. Sci. Comput.* **10**, 151–180.

Monin, A. S. & Yaglom, A. M. 1975 *Statistical Fluid Mechanics, Mechanics of Turbulence*, Vol 2. MIT press.

Mydlarski, L. & Warhaft, Z. 1998 Passive scalar statistics in high-Peclet-number grid turbulence. *J. Fluid Mech.* **358**, 135–175.

Obukhov, A. M. 1949 Structure of the temperature field in a turbulent flow. *Izv. Akad. Nauk. SSSR, Geogr. i Geofiz.* **13**, 58–69.

Obukhov, A. M. 1962 Some specific features of atmospheric turbulence. *J. Fluid Mech.* **13**, 77–81.

Prasad, R. R. & Sreenivasan, K. R. 1990 Quantitative three-dimensional imaging and the structure of passive scalar fields in fully turbulent flows. *J. Fluid Mech.* **216**, 1–34.

Praskovsky, A. A. 1992 Experimental verification of the Kolmogorov refined similarity hypothesis. *Phys. Fluids* A **4**, 2589–2591.

Pumir, A. 1994 Small-scale properties of scalar and velocity differences in three-dimensional turbulence. *Phys. Fluids* **6**, 3974–3984.

Ruetsch, G. R. & Maxey, M. R. 1992 The evolution of small-scale structures in homogeneous isotropic turbulence. *Phys. Fluids* A **4**, 2747–2760.

Sreenivasan, K. R. 1996 The passive scalar spectrum and the Obukhov-Corrsin constant. *Phys. Fluids* **8**, 189–196.

Sreenivasan, K. R. & Antonia, R. A. 1997 The phenomenology of small-scale turbulence. *Ann. Rev. Fluid Mech.* **29**, 435–472.

Sreenivasan, K. R., Antonia, R. A. & Danh, H. Q. 1977 Temperature dissipation fluctuations in a turbulent boundary layer. *Phys. Fluids* **20**, 1238–1249.

Stolovitzky, G., Kailasnath, P. & Sreenivasan, K. R. 1992 Kolmogorov's refined similarity hypotheses. *Phys. Rev. Lett.* **69**, 1178–1181.

Stolovitzky, G., Kailasnath, P. & Sreenivasan, K. R. 1995 Refined similarity hypotheses for passive scalars mixed by turbulence. *J. Fluid Mech.* **297**, 275–291.

Sullivan, N. P., Mahalingam, S. & Kerr, R. M. 1994 Deterministic forcing of homogeneous, isotropic turbulence. *Phys. Fluids* **6**, 1612–1614.

Tatarskii, V. I., Dubovikov, M. M., Praskovsky, A. A. & Karyakin, M. Y. 1992 Temperature fluctuation spectrum in the dissipation range for statistically isotropic turbulent flow. *J. Fluid Mech.* **238**, 683–698.

Thoroddsen, S. T. & Van Atta, C. W. 1992*a* Experimental evidence supporting Kolmogorov's refined similarity hypothesis. *Phys. Fluids* A **4**, 2592–2594.

Thoroddsen, S. T. & Van Atta, C. W. 1992*b* Exponential tails and skewness of density gradient PDFs in stably stratified turbulence. *J. Fluid Mech.* **244**, 547–566.

Van Atta, C. W. 1971 Influence of fluctuations in local dissipation rates on turbulent scalar characteristics in the inertial subrange. *Phys. Fluids* **14**, 1803–1804. Also Erratum *Phys. Fluids* **16**, 574 (1973).

Wang, L.-P., Chen, S., Brasseur, J. G. & Wyngaard, J. C. 1996 Examination of hypothesis in the Kolmogorov refined turbulence theory through high-resolution simulations. Part 1. velocity field. *J. Fluid Mech.* **309**, 113–156.

Wang, L.-P. & Maxey, M. R. 1993 Kinematical Descriptions for Mixing in Stratified or Homogeneous Shear Flows. In *Mixing in Geophysical Flows – Effects of Body Forces in Turbulent Flows* (ed. M. Redondo & O. Metais). Kluwer.

Warhaft, Z. & Lumley, J. L. 1978 An experimental study of the decay of temperature fluctuations in grid-generated turbulence. *J. Fluid Mech.* **88**, 659–684.

Williams, R. M. & Paulson, C. A. 1977 Microscale temperature and velocity spectra in the atmospheric boundary layer. *J. Fluid Mech.* **83**, 547–567.

Wyngaard, J. C. 1971 The effect of velocity sensitivity on temperature derivative statistics in isotropic turbulence. *J. Fluid Mech.* **48**, 763–769.

Yaglom, A. M. 1949 On the local structure of a temperature field in a turbulent flow. *Dokl. Akad. Nauk. SSSR* **69**, 743–746.

Yakhot, V. & Orszag, S. A. 1986 Renormalization group analysis of turbulence. I. Basic theory. *J. Sci. Comput.* **1**, 3–51.

Yeung, P. K. & Zhou, Y. 1997 Universality of the Kolmogorov constant in numerical simulations of turbulence. *Phys. Rev.* E **56**, 1726–1752.

Zhu, Y., Antonia, R. A. & Hosokawa, I. 1995 Refined similarity hypotheses for turbulent velocity and temperature fields. *Phys. Fluids* **7**, 1637–1648.